IEEE Access
Multidisciplinary ⋮ Rapid Review ⋮ Open Access Journal

Received 17 July 2024, accepted 18 August 2024, date of publication 21 August 2024, date of current version 2 September 2024.

Digital Object Identifier 10.1109/ACCESS.2024.3447531

RESEARCH ARTICLE

Enhancing Secrecy Performance Using Fountain Codes and NOMA Under Joint Cooperative Jamming Technique and Intelligent Reflective Surface

PHU TRAN TIN[1], (Member, IEEE), MINH-SANG VAN NGUYEN[2], TRAN TRUNG DUY[2], (Member, IEEE), BUI VU MINH[3], BYUNG-SEO KIM[4], (Senior Member, IEEE), AND LUBOS REJFEK[5]

[1]Data Science Laboratory, Faculty of Information Technology, Ton Duc Thang University, Ho Chi Minh City 70000, Vietnam
[2]Department of Electrical Engineering, Posts and Telecommunications Institute of Technology, Ho Chi Minh City 70000, Vietnam
[3]Faculty of Engineering and Technology, Nguyen Tat Thanh University, Ho Chi Minh City 754000, Vietnam
[4]Department of Software and Communications Engineering, Hongik University, Sejong 30016, South Korea
[5]FEI, University of Pardubice, 53210 Pardubice, Czech Republic

Corresponding author: Byung-Seo Kim (jsnbs@hongik.ac.kr)

This work was supported in part by Vietnam National Foundation for Science and Technology Development (NAFOSTED) under Grant 102.04-2021.57; and in part by Culture, Sports and Tourism R&D Program through the Korea Creative Content Agency grant funded by the Ministry of Culture, Sports and Tourism in 2024 (Project Name: Global Talent Training Program for Copyright Management Technology in Game Contents, Project Number: RS-2024-00396709, Contribution Rate: 100%).

ABSTRACT Ensuring content security and copyright protection is a critical concern in wireless communication networks. Furthermore, the emergence of services demanding high-band width and very low delay such as online Games, extended reality (XR), Metaverses, etc., Non-Orthogonal Multiple Access (NOMA) is a technology with the potential to enhance the spectral efficiency of fifth-generation (5G) wireless network and beyond. Hence, this paper studies a NOMA-based downlink system that employs intelligent reconfigurable surfaces (IRS) and operates in a physical-layer security environment. Our study also incorporates the utilization of Fountain codes (FCs), all while contending with the presence of a malicious eavesdropper. Furthermore, a cooperative jamming technique is employed to degrade the quality of the eavesdropping channel. The main contribution of this paper is to derive precise closed-form expressions of outage probability (OP), energy efficiency (EE), intercept probability (IP), and average secrecy rate (ASR) for the proposed system. We also develop a Deep Neural Network (DNN) model to evaluate OP, IP, ASR and the average number of time slots (ATS). Subsequently, Monte Carlo simulations are presented as a means to validate the theoretical findings. The simulation results yield the following insights: i) Their primary purpose is to validate the analytical formulas. ii) This research significantly contributes to deepening our understanding of IRS-NOMA systems, providing a foundation for future investigations into practical implementations. iii) We investigate the optimal power allocation factors within the IRS-NOMA framework, offering valuable insights into designing IRS-NOMA systems to achieve reliable and secure communication. iv) The results illustrate the superior performance of IRS-NOMA in comparison to the conventional IRS-Orthogonal Multiple Access (OMA) method.

INDEX TERMS Fountain codes, content security, intelligent reflecting surface, non-orthogonal multiple access, physical layer security.

I. INTRODUCTION

The emergence of the beyond fifth generation (B5G) and the subsequent development of the sixth generation (6G)

The associate editor coordinating the review of this manuscript and approving it for publication was Wei Wang.

wireless communications have ushered in a new era of possibilities for wireless networks across diverse domains [1], [2]. These advancements bring with them the promise of significantly higher data transmission speeds, enhanced operational efficiency, and the potential for groundbreaking applications. Furthermore, services requiring high bandwidth and very low delay such as online games, extended reality (XR), Metaverse, etc., can be supported over wireless connections. However, with these remarkable advancements, the rising demands of the general public may introduce new vulnerabilities in secure content and information deliveries in wireless networks.

In response to these evolving challenges, a technology that has garnered considerable attention, and holds promise for mitigating some of these security concerns is intelligent reconfigurable surfaces (IRS) [2], [3], [4]. An IRS comprises many low-cost reconfigurable passive components, each capable of manipulating the amplitude and phase of incoming signals [5]. The utilization of IRS is now being recognized as a cost-effective solution to substantially enhance the spectrum and energy efficiency (EE) of forthcoming wireless communication networks [6]. In [7] and [8], particular emphasis is given to IRS technology, notable for its remarkable potential to achieve substantial reductions in energy consumption. IRSs have garnered attention from both academic and industrial sectors, sparking intensive research efforts. Their capacity to contribute to energy-efficient communication systems has made them a focal point of interest and investigation within the field [9]. Moreover, several studies have studied the integration of Nakagami-m fading channels into internet of things (IoT) systems with RIS [10], [11], [12], [13]. In [10], the distribution of the sum of double-Nakagami-m random vectors is analyzed, providing exact closed-form expressions for the probability density function (PDF), cumulative distribution function (CDF), moments, and characteristic function. These statistical properties are also derived for the sum of Rayleigh-Nakagami-m random vectors. In [11], the impact of aerial IRS on data collection is examined by deriving outage probability (OP) for randomly deployed devices, considering both imperfect channel state information and unmanned aerial vehicles (UAV) fluctuations. Building on this, [12] investigates IRS-assisted device-to-device (D2D) communication under Nakagami-m fading, discussing both overlay and underlay modes. Novel closed-form analytical expressions for outage probability are derived for each mode, along with the diversity order. The findings reveal that in the overlay D2D mode, the diversity order depends on the number of elements and fading parameters, whereas in the underlay D2D mode, it is zero due to interference.

Non-Orthogonal Multiple Access (NOMA) emerges as a pivotal technique, especially in the context of B5G massive IoT [14], [15], [16]. NOMA enables the simultaneous utilization of the same time and frequency slot for two users by adjusting their power allocation levels. Unlike traditional orthogonal multiple access (OMA) schemes like Time Division Multiple Access (TDMA) and Frequency Division Multiple Access (FDMA), where each user is assigned time or frequency slots, NOMA facilitates multiple users to share resources concurrently, resulting in increased spectral efficiency and enhanced capacity. This enhancement is made possible by allocating different power levels to users, assigning higher power levels to those with weaker channel conditions and lower power levels to those with stronger conditions. Hence, such power allocation optimization aims at maximizing the overall system capacity. Moreover, numerous studies have presented combination between NOMA and other advanced wireless communication techniques [5], [6], encompassing OMA, millimeter-wave (mmWave) communication, UAV communications, and satellite communications. These models provide insights into the potential applications and benefits of IRS technology in enhancing system capacity, fairness, energy efficiency, and security.

In the realm of Physical Layer Security (PLS), various strategies are employed to safeguard wireless communication systems against eavesdropping and unauthorized access. One efficient technique in PLS is jamming, which operates by deliberately introducing noise or interference into the communication channel, thereby disrupting the reception of signals by eavesdroppers [17], [18], [19]. Furthermore, jamming can be dynamically adjusted in real time to adapt to evolving threats, offering a robust defense mechanism against sophisticated adversaries. In contrast to encryption techniques which may incur computational overhead and latency, jamming imposes minimal processing demands and can be seamlessly integrated into existing communication infrastructures. Thus, jamming emerges as a compelling PLS strategy, offering a potent combination of effectiveness, adaptability, and efficiency in safeguarding wireless communication systems against unauthorized access and exploitation [20], [21], [22].

Fountain codes (FCs) offer a promising solution for reliable data transmission in wireless communication. Unlike traditional codes, they generate an unlimited number of encoded symbols from a finite set, adapting dynamically to changing channel conditions [23], [24]. This adaptability makes them ideal for environments with variable noise and interference levels. FCs also boast resilience to burst errors and achieve high performance with minimal computational complexity. Their versatility extends across various applications, including satellite communication, multimedia streaming, and distributed storage systems. As a result, FCs have gained traction as an efficient and adaptable error correction technique in wireless communication [25]. Moreover, FCs belong to a family of linear block codes renowned for their ability to generate potentially unlimited encoded packets [26], [27], [28]. Among these, systematic FCs, exemplified by RaptorQ codes [29], have found widespread adoption as Application-Layer Forward Error Correction (AL-FEC) codes within the 3GPP Multimedia Broadcast and Multicast Services (MBMS) standard. This

is primarily due to their exceptional coding performance. In a related context, a study presented in [30] highlighted that systems relying solely on pure physical-layer coding, without the assistance of AL-FEC coding, are significantly suboptimal when operating in wireless fading channels. In the pursuit of achieving reliable packet transmission over wireless links, the proposed layered coding approach not only addresses error correction within each packet and erasure correction across packets but also emphasizes the security-enhancing benefits of FCs. The inherent resilience of FCs to packet loss contributes to an improved security posture, ensuring data integrity and reliable communication in wireless environments prone to disruptions or adversarial interference. This underscores the critical role of AL-FEC codes in enhancing communication reliability and robustness. Moreover, in [31], researchers introduced a cross-layer optimization approach. This approach involves the joint selection of Raptor code parameters at the application layer and physical layer coding parameters. The goal is to enhance transmission efficiency, particularly for unicast streaming of high-quality video. By optimizing parameters across multiple layers of the communication stack, this approach aims to deliver a more efficient and reliable streaming experience.

A. MOTIVATION

Due to the significant potential of integrating NOMA with IRS and the current research trend of incorporating deep neural networks (DNN) into system models, coupled with the enhancement of system performance and security through the integration of FCs in data transmission, it is imperative to address these areas. Security concerns have always been a top research priority to ensure signal transmission integrity. Therefore, designing a jammer device to mitigate eavesdropping effects is also a highly effective measure. However, there is a scarcity of studies addressing these issues comprehensively. In [32] and [36], the authors investigated the IRS-NOMA system model focusing on system performance and security analysis. Their model included signal transmission to two users, with one near user receiving a direct transmission from the base station (*BS*) and one far user receiving transmission via the IRS, in the presence of an eavesdropper. Nonetheless, these models did not consider scenarios where all users are served via the IRS, nor did it address eavesdropping through the IRS. Additionally, the impact of a jammer device on the system performance was not considered. In this paper, we have addressed the aforementioned issues. Moreover, we have also incorporated DNN techniques and applied FCs in the considered system.

In [23], a cross-layer design for a FCs two-user NOMA system with finite blocklength is proposed to achieve high reliability and low latency. Messages are encoded with application-layer fountain codes and physical-layer channel codes, then transmitted using superposition modulation. Numerical analysis shows that this design significantly reduces transmission latency compared to using only physical-layer channel codes. In [24], redundancy allocation between packet-level fountain coding and physical-layer channel coding in a downlink NOMA system with Rayleigh fading channels is optimized, maximizing overall code rates while ensuring successful decoding for both users. Numerical results highlight the importance of rapidly increasing the code rate for the weaker user to maximize overall rates, with minimal redundancy needed for fountain coding when transmit power is high and channel gain differences are small. However, these studies have not yet considered incorporating IRS into the system model, nor have they addressed security issues, integrated DNN, or implemented jammer devices.

In [37], the authors study transmit power control in mobile communication systems using a recurrent neural network (RNN) to maximize system capacity. Their proposed scheme reduces the need for extensive pilot signals in dense networks. Simulation results show that their approach outperforms conventional power control techniques and other neural network-based methods, as evidenced by lower mean square error and higher overall system capacity. In [38], a deep learning method is proposed for the online wireless configuration of IRSs in indoor environments. A coordinate fingerprint database is created during offline training to train a DNN, which maps user locations to optimal IRS configurations for maximizing signal strength. In the online phase, the DNN uses real-time location data to optimize IRS phases. Simulations show this method significantly increases throughput at the target user location. However, it is noted that, unlike the aforementioned works [37], [38], this paper studies the application of DNN to predict and optimize key performance metrics, specifically outage probability (OP), intercept probability (IP), and average secrecy rate (ASR). By leveraging the capabilities of DNNs, the study aims to enhance the accuracy and efficiency of these predictions and optimizations. The DNN model is trained on a comprehensive dataset to learn the complex relationships between various input parameters and performance metrics. Once trained, the DNN can efficiently predict OP, IP, and ASR under different conditions, providing valuable insights and enabling the optimization of network performance. This approach demonstrates the potential of DNNs in handling complex prediction and optimization tasks in communication systems, leading to improved reliability and efficiency.

Generally speaking, it is necessary to investigate IRS-aided systems relying on PLS in four key domains: (i) the emergence of IRS raises a significant challenge: How can we integrate IRS into the NOMA-based wireless systems to ensure that the reflected signals are constructive for the intended NOMA users?; (ii) how can we apply FCs to enhance the security and performance of the system?; (iii) how can we integrate the jamming techniques into IRS-NOMA systems to further enhance security?; (iv) how can a DNN-based optimization contribute to predicting system outcomes, thereby reducing computational complexity and increasing accuracy in practical applications? Therefore,

TABLE 1. A comparison between related works and the current study.

	Our research	[20]	[28]	[32]	[33]	[17]	[19]	[34]	[35]
IRS-OMA system	√	√		√				√	√
IRS-NOMA system	√			√					
FCs	√		√		√				
Cooperative jamming	√	√				√	√		
PLS	√	√		√	√	√		√	√
DNN	√					√			
Multiple users	√								
OP	√	√	√	√			√		
EE	√		√						
ATS	√								
IP	√	√		√	√				
ASR	√			√				√	

"√" provides references that delve into this topic extensively.

this paper aims to study the secure performance and overall efficiency of IRS-NOMA-aided IoT systems.

B. CONTRIBUTIONS

Inspired by the above discussion, this paper studies a novel secure communication system that effectively leverages the unique properties of FCs. Unlike the existing approaches, our system ensures that encoded packets are used to enhance security, making it difficult for eavesdroppers to intercept a sufficient number of packets to decode the original data. Specifically, the proposed system allows a *BS* to transmit encoded packets to multiple users via the IRS-NOMA technique. Furthermore, users send feedback to the *BS* once they have received enough encoded packets to decode the original data. This ensures that secure transmission relies on users receiving enough encoded packets before eavesdroppers can do so, thereby fully exploiting the unique characteristics of FCs. The main contributions of this paper can be concisely described as follows:

- A novel secure communication protocol is introduced, effectively leveraging the unique properties of FCs. Unlike the existing approaches, this protocol ensures that the encoded packets enhance security, making it difficult for eavesdroppers to intercept a sufficient number of packets to decode the original data.
- The IRS-based NOMA system is proposed, where the *BS* communicates with user 1 (D_1) and user 2 (D_2) through the IRS. The proposed system also addresses the challenge of potential eavesdroppers. To mitigate this security risk, the system incorporates a jamming device to disrupt the eavesdroppers' ability to intercept the data. This approach not only leverages FCs but also innovates by integrating jamming techniques to degrade the eavesdropping channel quality.
- This paper presents a comprehensive evaluation of the PLS of the proposed system, leveraging FCs. It derives analytical expressions for key performance metrics, including OP, EE, and the average number of time slots (ATS). Furthermore, it assesses the IP and the ASR necessary for secure communication among legitimate users (D_1 and D_2) and potential eavesdroppers. By incorporating FCs, this thorough evaluation ensures a robust analysis of both reliability and security aspects, highlighting the benefits of FCs in enhancing communication security. Moreover, we have extended the IRS-NOMA model by considering the impact of multiple users. Specifically, we have conducted simulations for the OP case and evaluated their outcomes.
- Unlike the previous studies, our proposed IRS-based NOMA system leverages both FCs and DNN techniques to evaluate the OP, ASR, and IP. The DNN model, combined with the properties of FCs, serves as an efficient tool for assessing system performance, especially when closed-form analytical expressions are challenging to obtain. This approach simplifies the complexity associated with evaluating highly nonlinear functions, providing accurate estimations of system performance metrics. Thus, the application of DNN and FCs is not superficial but deeply integrated into performance evaluation.
- Extensive simulations are conducted to validate the theoretical analysis and gain valuable technical insights. The effectiveness of the DNN model, combined with the application of FCs, is evaluated using the mean squared error (MSE) metric and compared with conventional approaches. Furthermore, various other results are examined to confirm the benefits of integrating IRS, NOMA, and FCs in enhancing the system performance, particularly in scenarios with potential eavesdroppers. Finally, the optimal performance of the OP is determined accordingly.

C. ORGANIZATION AND NOTATIONS

The paper is divided into the 06 sections. The proposed system paradigm is examined in Section II. Section III provides an overview of the methodology and the analyzes of secrecy performance. In Section IV, we introduce the DNN model for estimating the OP performance. Section V presents an extended case for multiple users within the considered system. On the basis of the DNN model predictions and the derived analytical results, we show representative numerical results in Section VI. This paper is concluded in Section VII.

Notations: In this paper, we represent scalars using italicized letters, while vectors and matrices are indicated by boldface letters. For a vector $\mathbf{z}$, the notation diag $[\mathbf{z}]$ refers to a diagonal matrix in which each diagonal element corresponds to the elements of vector $\mathbf{z}$, respectively. The notation $\mathbf{z}^T$ represents the transpose of vector $\mathbf{z}$. arg (.) represents the argument of a complex number. Pr (.) and E (.) signify the probability and the expectation, respectively. A complex circular symmetric Gaussian random variable with a zero mean and a variance of λ is denoted as $CN\ (0, \lambda)$. The CDF and PDF of the random variable Y are denoted by $F_Y\ (y)$ and $f_Y\ (y)$, respectively.

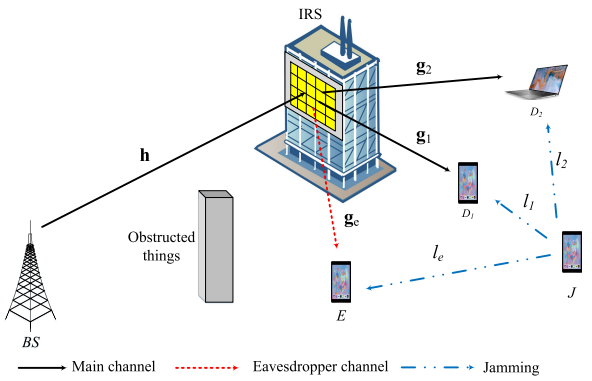

FIGURE 1. The IRS downlink system model.

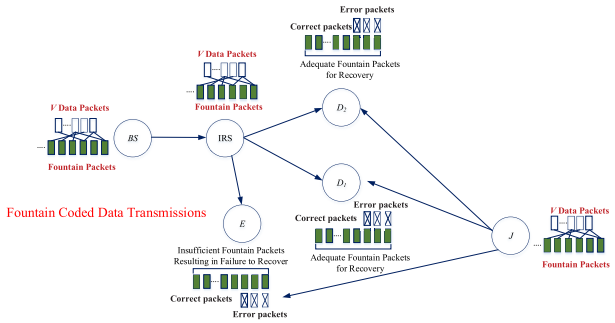

FIGURE 2. Fountain-encoded transmission for security.

II. SYSTEM MODEL

The IRS-based downlink NOMA network is shown in Figure 1. It comprises a *BS*, an IRS with N reflecting elements, and two receivers,[1] D_i, $(i = 1, 2)$. An eavesdropper (E) is listening to the network while it is in use. More specifically, D_1 and D_2 are the users who need an IRS's help to communicate because of the far distance and obstacles. In addition, D_1 is a user who is closer to the IRS than user D_2. The cooperative jamming technique is used to degrade the quality of the eavesdropping link, i.e., the jammer (J) is employed to continuously generate the artificial noises to E.

The *BS* partitions its initial data into V packets, ensuring their proper encoding to yield the encoded packets. Subsequently, during each time slot, the *BS* transmits these encoded packets individually to the D_i. Concurrently, the E tries to intercept the encoded packets. It is assumed that both the D_i and the E achieve successful retrieval of the original data upon correctly capturing a minimum of G encoded packets, where $G = (1+\alpha)\,V$, and α is the decoding overhead which depends on concrete code design [28], [33], [40]. Furthermore, once the D_i accumulates enough number of encoded packets, it issues an ACK message, prompting the *BS* to terminate the data transmission. If the eavesdropper fails to capture enough encoded packets, it remains incapable of accessing the *BS* data. Conversely, the eavesdropper intercepts the original *BS* data. Moreover, Figure 2 depicts the FCs technique utilized in the system model [24].

Furthermore, we assume that the N reflecting elements of the IRS will be divided into $N = N_1 + N_2$ [41], where N_1 elements are set to steer towards user D_1, and the remaining N_2 elements are set to steer towards user D_2; the reflection coefficient matrix associated with the *BS*-IRS-D_i and *BS*-IRS-E are symbolized by $\Phi_i = \text{diag}\left[\delta_1 e^{j\phi_1^i}, \delta_2 e^{j\phi_2^i}, \ldots, \delta_{N_i} e^{j\phi_{N_i}^i}\right]$, $\Phi_e = \text{diag}\left[\delta_1 e^{j\phi_1^e}, \delta_2 e^{j\phi_2^e}, \ldots, \delta_{N_i} e^{j\phi_c^e}\right]$, $\left(j = \sqrt{-1}\right)$, $c \in \{N_1, N_2\}$, where $\delta_{N_i} \in [0, 1]$ is the amplitude-reflection coefficient, the assumption that $\delta = \delta_1 = \delta_2 = \cdots = \delta_{N_i}$ [42], and $\phi_{n_i}^i \in [0, 2\pi)$ represents the adjustable phase shift variable of the n_i-th element, which can be controlled by the IRS with $n_i = (1, \ldots, N_i)$. The Rayleigh fading model[2] characterizes the small-scale fading for both the link from J to D_i and the link from J to E, and these are represented by $l_i \sim CN\left(0, \lambda_{l_i}\right)$, and $l_e \sim CN\left(0, \lambda_{l_e}\right)$, respectively. Particularly, $\mathbf{h} = [h_1, h_2, \ldots, h_c]$, $\mathbf{g}_1 = \left[g_{1,1}, g_{1,2}, \ldots, g_{1,N_1}\right]^T$, and $\mathbf{g}_2 = \left[g_{2,1}, g_{2,2}, \ldots, g_{2,N_2}\right]^T$, $\mathbf{g}_e = \left[g_{e,1}, g_{e,2}, \ldots, g_{e,c}\right]^T$ represent the complex channel coefficients corresponding to *BS*-IRS, IRS-D_1, IRS-D_2, and IRS-E, respectively. Each element within $\mathbf{h}$ and $\mathbf{g}_i$ conforms to the Nakagami-m fading

[1]The two-user IRS-NOMA emerges as the prime choice, acclaimed for its exceptional spectral efficiency and amplified user fairness, extensively supported by prior research [36], [39]. By allocating distinct power levels according to priority based on individual channel conditions, it not only amplifies system capacity but also guarantees fair service distribution among users, establishing itself as a compelling solution within contemporary wireless communication systems. We focus on the secure performance of a user pair because the performance characteristics for other groups are similar. In the context of an IoT user pair, one user may send high-data-rate videos while the other sends low data rate text messages. The motivation includes ensuring high-quality service, testing scalability, and identifying potential issues early. This system model is suitable for multimedia communication applications, social networking platforms, collaborative tools, online gaming, and IoT systems.

[2]The jamming links are considered as Rayleigh instead of Nakagami-m because the Rayleigh fading model is a common and widely accepted assumption for modeling wireless channels in environments with many scatterers, such as urban areas [17], [19]. This model is particularly suitable when there is non line-of-sight (NLOS) path. On the other hand, the Nakagami-m fading model, which generalizes the Rayleigh model (m= 1) [19], is often used to model scenarios with varying degrees of LOS and multipath fading. In this paper, we assume the jamming links are represented by the Rayleigh model due to the specific characteristics of the environment we are considering. However, we acknowledge that using Nakagami-m could be an alternative approach and may be explored in future work.

model,[3] with distinct fading parameters, namely m_h and m_{g_i}, respectively. We assume that the channel coefficients do not change during the transmission of one Fountain packet, and they change independently after each transmission of one Fountain packet.

Let W represent the length of each encoded packet. If the BS transmits the signal $x_{s_i}[w]$, $(w = 1, \ldots, W)$ to the D_i. Assume that BS sends the packets $c_1[l]$ (denotes the l-th packets of D_1) and $c_2[l]$ (denotes the l-th packets of D_2) to D_1 and D_2, $(l = 1, 2, \ldots)$, respectively. Following the NOMA principle, BS linearly combines the modulated signals of $c_1[l]$ and $c_2[l]$ as $x_s[w] = \sqrt{\beta_1 P_s} x_{s_1}[w] + \sqrt{\beta_2 P_s} x_{s_2}[w]$, where P_s (dB) represents the transmit power of the BS, and $x_{s_1}[w]$ and $x_{s_2}[w]$ represent the transmitted signals of the w-th symbol of $c_1[l]$ and $c_2[l]$, respectively. Additionally, β_i is used to denote the power allocation coefficients for D_i, with $\beta_1 + \beta_2 = 1$ and $\beta_i \in [0, 1]$. Be aware that we set $\beta_1 < \beta_2$ for user fairness and assume fixed power allocation sharing between two users [44]. The received signal at D_1 is provided by [36], [45]

$$y_{D_1}^N = d_s^{-\frac{\eta}{2}} d_{r_1}^{-\frac{\eta}{2}} \mathbf{g}_1 \Phi_1 \mathbf{h} x_s[w] + d_{J_1}^{-\frac{\eta}{2}} \sqrt{P_{Ja}} l_1 x_{Ja}[w] + \sigma_1[w], \tag{1}$$

where d_s, d_{r_i} and d_{J_i} are the distances between the BS and IRS, between the IRS and D_i and between the J and D_i, respectively, η signifies the path loss exponents, $x_{Ja}[w]$ refers to the w-th jamming signal transmitted by nodes J, and P_{Ja} represents the transmit power of J. Additionally, $\sigma_i[w] \sim CN(0, N_0)$ is the additive white Gaussian noise (AWGN) at D_i, and N_0 is the variance.

At D_1, the initial detection prioritizes the signal from D_2, and the corresponding signal-to-interference-plus-noise ratio (SINR) is denoted by[4]

$$\gamma_{D_1}^{x_2} = \frac{d_s^{-\eta} d_{r_1}^{-\eta} \beta_2 \tau_s |\mathbf{g}_1 \Phi_1 \mathbf{h}|^2}{d_s^{-\eta} d_{r_1}^{-\eta} \beta_1 \tau_s |\mathbf{g}_1 \Phi_1 \mathbf{h}|^2 + d_{J_1}^{-\eta} \tau_{Ja} |l_1|^2 + 1}, \tag{2}$$

where $\tau_s = \frac{P_s}{N_0}$, $\tau_{Ja} = \frac{P_{Ja}}{N_0}$.

After the SIC process, the decoding of the signal from D_1 is realized, and the obtained SINR is given by

$$\gamma_{D_1}^{x_1} = \frac{d_s^{-\eta} d_{r_1}^{-\eta} \beta_1 \tau_s |\mathbf{g}_1 \Phi_1 \mathbf{h}|^2}{d_{J_1}^{-\eta} \tau_{Ja} |l_1|^2 + 1}. \tag{3}$$

[3]The justification for assuming Rayleigh fading and Nakagami-m fading, as highlighted in [34] and [35], arises from potential blockages on various links or suboptimal positioning of the IRS, which may compromise the establishment of robust LOS connections, thus enhancing the received signal strength. Additionally, Nakagami-m fading has the capability to replicate diverse wireless fading channels through the manipulation of channel fading parameters m [43].

[4]We assume D_1 is a near user to the BS and IRS, and D_2 is a user far to the BS and IRS [41]. In NOMA, the successive interference cancellation (SIC) is applied to decode the signal for D_1, as follows: first, decode the signal of the far user, D_2, then apply the SIC technique to decode D_1's own signal. For D_2, the SIC technique is not applied; D_2 only decodes its own signal and treats D_1's signal as interference.

Next, the signal received at D_2 can be expressed as

$$y_{D_2}^N = d_s^{-\frac{\eta}{2}} d_{r_2}^{-\frac{\eta}{2}} \mathbf{g}_2 \Phi_2 \mathbf{h} x_s[w] + d_{J_2}^{-\frac{\eta}{2}} \sqrt{P_{Ja}} l_2 x_{Ja}[w] + \sigma_2[w]. \tag{4}$$

At D_2, its signal is directly decoded (the D_1's signal is considered as noise), and the resulting SINR is then given by

$$\gamma_{D_2}^{x_2} = \frac{d_s^{-\eta} d_{r_2}^{-\eta} \beta_2 \tau_s |\mathbf{g}_2 \Phi_2 \mathbf{h}|^2}{d_s^{-\eta} d_{r_2}^{-\eta} \beta_1 \tau_s |\mathbf{g}_2 \Phi_2 \mathbf{h}|^2 + d_{J_2}^{-\eta} \tau_{Ja} |l_2|^2 + 1}. \tag{5}$$

The signal received by the E can be described as [35], [45]

$$y_E^N = d_s^{-\frac{\eta}{2}} d_{r_e}^{-\frac{\eta}{2}} \mathbf{g}_e \Phi_e \mathbf{h} x_s[w] + d_{J_e}^{-\frac{\eta}{2}} \sqrt{P_{Ja}} l_e x_{Ja}[w] + \sigma_e[w], \tag{6}$$

where d_{r_e} and d_{J_e} are to the distances from the IRS to E and from the J to E, respectively, $\sigma_e[w] \sim CN(0, N_e)$ represents the AWGN at E, and N_e is the variance.

In this study, like [46], [47], and [48], parallel interference cancellation (PIC) is employed at E to separate the superimposed mixture. Consequently, the corresponding SINR at E can be formulated as

$$\gamma_E^{x_i} = \frac{d_s^{-\eta} d_{r_e}^{-\eta} \beta_i \tau_e |\mathbf{g}_e \Phi_e \mathbf{h}|^2}{d_{J_e}^{-\eta} \tau_{Je} |l_e|^2 + 1}, \tag{7}$$

where $\tau_e = \frac{P_s}{N_e}$, $\tau_{Je} = \frac{P_{Ja}}{N_e}$.

III. PERFORMANCE ANALYSIS

This section mainly focuses on the performance analysis of our proposed systems from the perspectives of the OP, EE, IP, ASR, and ATS.

A. ANALYSIS OF OP

1) OP FOR D_1

In this paper, we assume that the SIC operation is perfect, and if D_1 is unable to decode the encoded packet of $x_{s_1}[w]$, this event is considered to be an outage. On the other hand, for $x_{s_1}[w]$ to be successfully decoded by D_1, two conditions must be met: i) D_1 successfully decodes $x_{s_2}[w]$, and 2) D_1 successfully decodes its own data $x_{s_1}[w]$. Therefore, the OP of one Fountain packet at D_1 can be expressed as [28], [49]

$$OP_{D_1} = 1 - \Pr\left(\gamma_{D_1}^{x_2} > \gamma_2^{th}, \gamma_{D_1}^{x_1} > \gamma_1^{th}\right), \tag{8}$$

where $\gamma_i^{th} = 2^{R_i} - 1$, R_i is the user D_i's target data rate.

Theorem 1: The exact expression of the OP at D_1 for one encoded packet is given by

$$OP_{D_1} = \exp\left(\frac{\omega}{\omega d_{J_1}^{-\eta} \tau_{Ja} \lambda_{l_1}} - \frac{\lambda_1}{2}\right) \times \sum_{m=0}^{\infty} \frac{\lambda_1^m}{m! 2^{m+1/2}} \left(\frac{\tau_s}{\omega d_{J_1}^{-\eta} \tau_{Ja} \lambda_{l_1}} + \frac{1}{2}\right)^{-(m+1/2)}, \tag{9}$$

where $\xi_1 = \frac{d_s^{-\eta} d_{r_1}^{-\eta} \delta^2}{N_1 (1-\varepsilon_1)}$, $\omega = \max\left(\frac{\gamma_2^{th}}{(\beta_2 - \gamma_2^{th} \beta_1) \xi_1}, \frac{\gamma_1^{th}}{\xi_1 \beta_1}\right)$.

Proof: Appendix A contains the comprehensive details. Due to the delay constraint, the number of time slots allocated or the number of Fountain packet transmissions by BS is limited. We denote M_{th} as the maximum number of transmission times for the BS, and M_{BS} as the number of transmission times that BS uses, where $M_{th} \geq M_{BS} \geq G$. This means that after M_{th} transmission times, BS stops the transmission, and the D_i will not be able to reconstruct the original data (or D_i is outage) if it does not receive a minimum of G encoded packets. We also denote M_{D_i} and M_E as number of Fountain packets successfully received by nodes D_i and E, respectively. If $M_{D_i} < G$, D_i is outage. Therefore, the OP of D_1 can be expressed as in [23]:

$$OP_{D_1}^{G} = \Pr\left(M_{D_1} < G \middle| M_{BS} = M_{th}\right). \tag{10}$$

Then, based on [23, Eq. (21)], we can obtain an exact formula of the OP of D_1 as

$$OP_{D_1}^{G} = \sum_{M_{D_1}=0}^{G-1} \binom{M_{th}}{M_{D_1}} \left(1 - OP_{D_1}\right)^{M_{D_1}} \times \left(OP_{D_1}\right)^{M_{th}-M_{D_1}}. \tag{11}$$

2) OP FOR D_2

For D_2, the OP of one encoded packet is expressed as in [50]:

$$OP_{D_2} = \Pr\left(\gamma_{D_2}^{x_2} < \gamma_2^{th}\right). \tag{12}$$

Similar to the steps for performing the OP calculation for D_1, the OP for D_2 with one Fountain packet is given by

$$OP_{D_2} = \exp\left(\frac{\gamma_2^{th}}{\gamma_2^{th} d_{J_2}^{-\eta} \tau_{Ja} \lambda_{l_2}} - \frac{\lambda_2}{2}\right) \times \sum_{m=0}^{\infty} \frac{\lambda_2^m}{m! 2^{2m+1/2}} \left(\frac{\left(\beta_2 - \gamma_2^{th}\beta_1\right)\xi_2 \tau_s}{\gamma_2^{th} d_{J_2}^{-\eta} \tau_{Ja} \lambda_{l_2}} + \frac{1}{2}\right)^{-(m+1/2)}, \tag{13}$$

where $\xi_2 = \frac{d_s^{-\eta} d_{r_2}^{-\eta} \delta^2}{N_2(1-\varepsilon_2)}$.

Similar to (11), an exact closed-form expression of the OP at the D_2 can be written by

$$OP_{D_2}^{G} = \sum_{M_{D_2}=0}^{G-1} \binom{M_{th}}{M_{D_2}} \left(1 - OP_{D_2}\right)^{M_{D_2}} \times \left(OP_{D_2}\right)^{M_{th}-M_{D_2}}. \tag{14}$$

B. OPTIMIZING POWER ALLOCATION IN THE IRS-NOMA SYSTEM

In this section, we consider the optimization of power allocation to improve the performance of the proposed IRS-NOMA system. Firstly, we identify the optimal power allocation coefficients at the BS (denoted as β_1^*) to individually minimize the OP in the IRS-NOMA network. This task focuses on finding the power allocation coefficients of β_1^* at the BS that result in the lowest OP. To achieve this, we formulate the following minimization problems:

$$\underbrace{\min}_{\beta_1} OP_{D_i}^{G}(\beta_1), \quad \text{st.} \begin{cases} \beta_1 + \beta_2 = 1 \\ \beta_1 < \beta_2. \end{cases} \tag{15}$$

To determine β_1^*, we adopt the alternating optimization procedure [51] for numerical evaluation. The essential steps of this process are outlined in Algorithm 1. The procedure begins by selecting an initial feasible solution $\beta_1^{(0)}$ within the range (0,1), and then iteratively generates a sequence of optimized power allocation coefficients, denoted as $\beta_1^{(1)} \rightarrow \beta_1^{(2)} \rightarrow \cdots$. This approach allows us to find the jointly optimal value of β_1^* that minimizes $OP_{D_i}^{G}(\beta_1)$. The algorithm yields a sequence of $OP_{D_i}^{G}(\beta_1)$ values that are non-increasing. Notably, OP is a bounded function with $OP_{D_i}^{G}(\beta_1) \geq 0$, and the constraint set is convex. Thus, the convergence of a non-increasing sequence within a convex set with a bounded objective function is guaranteed. Furthermore, it has been shown that $OP_{D_i}^{G}(\beta_1)$ is convex with respect to β_1 individually, ensuring that Algorithm 1 converges to the global optimal solution β_1^*.

Algorithm 1 Method for Identifying β_1^* Using an Alternating Optimization Approach

1: **Input:** Initialize the index $s = 0$ and set a tolerance level $\Delta > 0$. Choose an initial value $\beta_1^{(0)} \in (0, 1)$. Calculate the initial performance metric $\partial^{(0)} = OP_{D_i}^{G}(\beta_1^{(0)})$.
2: **Output:** The optimal value of β_1^* that minimizes the outage performance, $OP_{D_i}^{G}(\beta_1^*)$
3: To determine the optimal β_1, set $\beta_1 = \beta_1^{(s)}$ and solve equation (15).
4: Compute $\partial^{(s+1)} = OP_{D_i}^{G}\left(\beta_1^{(s+1)}\right)$, and $\partial^* = \partial^{(s+1)}$
5: **Set** $\beta_1^* = \beta_1^{(s+1)}$
6: **Until** $\left|\partial^{(s+1)} - \partial^{(s)}\right| \leq \Delta$
7: **Else** $s = s + 1$
8: Proceed to step 2

C. ANALYSIS OF EE

Building on the outage performance, we evaluate throughput within the constraints of delay-limited transmission mode. In this context, throughput represents the system's capacity at a fixed data rate. Indeed, the system throughput for IRS-NOMA in delay-limited transmission mode can be expressed as in [52, Eq. (21)] as

$$TP_{Sy} = (1 - OP_1) R_1 + (1 - OP_2) R_2. \tag{16}$$

In the IRS-NOMA system, the overall power usage includes the BS's transmitting power, the static power consumed by hardware at the BS, IRS, and user terminals [53]. This can be

formulated as [52, Eq. (33)]:

$$P_{tong} = \frac{P_s}{\varepsilon} + P_{bs} + P_I + P_{D_1} + P_{D_2} + P_{Ja}, \tag{17}$$

where ε represents the efficacy of the power amplifier in transmission. P_{bs} denotes the cumulative hardware static power dissipation at the BS, while $P_I = NP_n(a)$ signifies the corresponding power dissipation at the IRS, where $P_n(a)$ represents the energy usage of individual phase shifters, each operating at a a-bit resolution [54]. P_{D_i} represents the hardware power dissipation specific to the D_i. As throughput in the delay-limited transmission is acquired, there's a necessity for a more comprehensive study of EE in IRS-NOMA. The EE can be formulated as [52]:

$$\Upsilon = \frac{TP_{Sy}}{P_{tong}}. \tag{18}$$

D. ANALYSIS OF IP

From (7), we can formulate the IP of one Fountain packet of the user D_i as in [55]:

$$\begin{aligned} IP_{D_i} &= \Pr\left(\gamma_E^{x_i} > \gamma_i^{th}\right) \\ &= 1 - \Pr\left(|l_e|^2 > \frac{\xi_e \beta_i \tau_e \left(\sum_{n=1}^{c} |h_n| \left|g_{e,n}\right|\right)^2 - \gamma_i^{th}}{\gamma_i^{th} d_{J_e}^{-\eta} \tau_{Je}}\right) \\ &= 1 - \int_0^{\infty} \left(1 - F_{|l_e|^2}\left(\frac{\xi_e \beta_i \tau_e x - \gamma_i^{th}}{\gamma_i^{th} d_{J_e}^{-\eta} \tau_{Je}}\right)\right) \\ &\quad \times f_{\left(\sum_{n=1}^{c} |h_n||g_{e,n}|\right)^2}(x)\, dx, \end{aligned} \tag{19}$$

where $\xi_e = \frac{d_s^{-\eta} d_{re}^{-\eta} \delta^2}{c(1-\varepsilon_e)}$, $c \in \{N_1, N_2\}$.

Based on (35), (38), and by employing [56, Eq. (3.381.4)], IP_{D_i} can be derived as

$$\begin{aligned} IP_{D_i} &= 1 - \exp\left(\frac{\gamma_i^{th}}{\gamma_i^{th} d_{J_e}^{-\eta} \tau_{Je} \lambda_{l_e}} - \frac{\lambda_e}{2}\right) \\ &\quad \times \sum_{r=0}^{\infty} \frac{\lambda_e^r}{r! 2^{2r+1/2} \Gamma(r+1/2)} \\ &\quad \times \int_0^{\infty} x^{r+1/2-1} \exp\left(-\left(\frac{\xi_e \beta_i \tau_e}{\gamma_i^{th} d_{J_e}^{-\eta} \tau_{Je} \lambda_{l_e}} + \frac{1}{2}\right) x\right) dx \\ &= 1 - \exp\left(\frac{\gamma_i^{th}}{\gamma_i^{th} d_{J_e}^{-\eta} \tau_{Je} \lambda_{l_e}} - \frac{\lambda_e}{2}\right) \\ &\quad \times \sum_{r=0}^{\infty} \frac{\lambda_e^r}{r! 2^{2r+1/2}} \left(\frac{\xi_e \beta_i \tau_e}{\gamma_i^{th} d_{J_e}^{-\eta} \tau_{Je} \lambda_{l_e}} + \frac{1}{2}\right)^{-(r+1/2)}. \end{aligned} \tag{20}$$

It is worth noting that if E collects a sufficient number of G encoded packets before the BS's transmission ends, the data intended for D_i is intercepted. Hence, The IP of D_i can be formulated as [40]:

$$IP_{D_i}^G = \Pr\left(M_E = G \,|M_{BS} \le M_{th}\right). \tag{21}$$

Utilizing the binomial distribution's definition, the IP of D_i in (20) can be obtained as in [57, Eq. (9)]:

$$IP_{D_i}^G = \sum_{v=G}^{M_{th}} \binom{v-1}{v-G} \left(IP_{D_i}\right)^G \left(1 - IP_{D_i}\right)^{v-G}. \tag{22}$$

where v=M_{BS} is the number of Foutain-packet transmission times realized by BS.

Equation (22) implies that the eavesdropper E successfully receives G Fountain packets after v transmission times by BS. Therefore, it can intercept the the data intended for D_i.

E. ANALYSIS OF ASR

1) ASR FOR D_1

The ASR of D_1 with one Fountain packet is written as [58]

$$\begin{aligned} \overline{ASR}_{D_1} &= \mathrm{E}\left[\log_2\left(\frac{1+\gamma_{D_1}^{x_1}}{1+\gamma_E^{x_1}}\right)\right]^+ \\ &= \underbrace{\mathrm{E}\left[\log_2\left(1+\gamma_{D_1}^{x_1}\right)\right]}_{\Psi_1} - \underbrace{\mathrm{E}\left[\log_2\left(1+\gamma_E^{x_1}\right)\right]}_{\Psi_2}, \end{aligned} \tag{23}$$

where $[X]^+ = \max\{0, X\}$.

Theorem 3: The exact expression for the ASR at D_1 with one Fountain packet is given by

$$\begin{aligned} \overline{ASR}_{D_1} &= \frac{1}{\ln 2} \left[\sum_{m=0}^{\infty} \sum_{k=1}^{K} \frac{\lambda_1^m \sqrt{1-t_k^2}}{m! 2^m \Gamma(m+1/2)} \frac{Q\pi \exp\left(-\frac{\lambda_1}{2} - \frac{\Xi}{\lambda_{l_1}}\right)}{2K\lambda_{l_1}} \right. \\ &\quad \times G_{2,3}^{3,1}\left(\begin{matrix} 0, 1 \\ 0, m+\frac{1}{2}, 0 \end{matrix} \middle| \frac{\left(d_{J_1}^{-\eta} \tau_{Ja} \Xi + 1\right)}{2\xi_1 \beta_1 \tau_s}\right) \\ &\quad - \sum_{m=0}^{\infty} \sum_{k=1}^{K} \frac{\lambda_e^m \sqrt{1-t_k^2}}{m! 2^m \Gamma(m+1/2)} \frac{Q\pi \exp\left(-\frac{\lambda_e}{2} - \frac{\Xi}{\lambda_{l_e}}\right)}{2K\lambda_{l_e}} \\ &\quad \left. \times G_{2,3}^{3,1}\left(\begin{matrix} 0, 1 \\ 0, m+\frac{1}{2}, 0 \end{matrix} \middle| \frac{\left(d_{J_e}^{-\eta} \tau_{Je} \Xi + 1\right)}{2\xi_e \beta_1 \tau_e}\right)\right], \end{aligned} \tag{24}$$

where $\Xi = \frac{Qt_k + Q}{2}$, $t_k = \cos\left[\frac{(2k-1)\pi}{2K}\right]$, K is a trade-off parameter for accuracy and complexity.

Proof: You can find the information in Appendix B.

2) ASR FOR D_2

The ASR of D_2 with one Fountain packet can be written as

$$\begin{aligned} \overline{ASR}_{D_2} &= \mathrm{E}\left[\log_2\left(\frac{1+\gamma_{D_2}^{x_2}}{1+\gamma_E^{x_2}}\right)\right]^+ \\ &= \underbrace{\mathrm{E}\left[\log_2\left(1+\gamma_{D_2}^{x_2}\right)\right]}_{\Psi_3} - \underbrace{\mathrm{E}\left[\log_2\left(1+\gamma_E^{x_2}\right)\right]}_{\Psi_4}. \end{aligned} \tag{25}$$

Theorem 4: The exact expression for the ASR at D_2 with one Fountain packet is given by

$$\overline{ASR}_{D_2} = \frac{1}{\ln 2}\left[\sum_{m=0}^{\infty}\sum_{k=1}^{K}\sum_{u=1}^{U}\frac{\lambda_2^m\sqrt{1-t_k^2}\sqrt{1-z_u^2}}{m!2^m\Gamma\left(m+1/2\right)} \times \frac{\beta_2 Q\pi\pi\exp\left(-\frac{\lambda_2}{2}-\frac{\Xi}{\lambda_{l_2}}\right)}{4\beta_1 KU\lambda_{l_2}\left(1+\Theta\right)} \Gamma\left(m+\frac{1}{2},\frac{\Theta\left(d_{J_2}^{-\eta}\tau_{Ja}\Xi+1\right)}{2\left(\beta_2-\Theta\beta_1\right)\xi_2\tau_s}\right) - \sum_{m=0}^{\infty}\sum_{k=1}^{K}\frac{\lambda_e^m\sqrt{1-t_k^2}}{m!2^m\Gamma\left(m+1/2\right)}\frac{Q\pi\exp\left(-\frac{\lambda_e}{2}-\frac{\Xi}{\lambda_{l_e}}\right)}{2K\lambda_{l_e}} \times G_{2,3}^{3,1}\left(\begin{matrix}0,1\\0,m+\frac{1}{2},0\end{matrix}\middle|\frac{\left(d_{J_e}^{-\eta}\tau_{Je}\Xi+1\right)}{2\xi_e\beta_2\tau_e}\right)\right], \quad (26)$$

where $z_u = \cos\left[\frac{(2u-1)\pi}{2U}\right]$, $\Theta = \frac{\beta_2 z_u+\beta_2}{2\beta_1}$, U is a trade-off parameter for accuracy and complexity.

Proof: Consult Appendix C for the information.

F. ANALYSIS OF ATS

Theorem 5: The exact expression for the ATS at D_i, with the G Fountain packet requirement, are given by

$$ATS_{D_i} = \sum_{v=0}^{G-1} M_{th}\binom{M_{th}}{v}\left(1-OP_{D_i}\right)^v\left(OP_{D_i}\right)^{M_{th}-G} + \sum_{z=0}^{M_{th}} z\binom{z-1}{z-G}\left(1-OP_{D_i}\right)^G\left(OP_{D_i}\right)^{z-G}. \quad (27)$$

Proof: The ATS employed for sending encoded packets to the D_i can be formulated as:

$$ATS_{D_i} = \underbrace{\sum_{v=0}^{G-1} M_{th}\Pr\left(M_{D_i}=v\,|M_{BS}=M_{th}\right)}_{\Delta_1} + \underbrace{\sum_{z=G}^{M_{th}} z\Pr\left(M_{D_i}=G\,|M_{BS}=z\right)}_{\Delta_2}. \quad (28)$$

In (28), Δ_1 presents the case where D_i is outage, and the number of transmission times that BS uses is M_{th}. For Δ_2, it presents the case where D_i successfully recovers its data within z transmission times realized by BS.

In a similar manner to (11) and (22), Δ_1 and Δ_2 can be rephrased as follows:

$$\Delta_1 = \sum_{v=0}^{G-1} M_{th}\binom{M_{th}}{v}\left(1-OP_{D_i}\right)^v\left(OP_{D_i}\right)^{M_{th}-G}, \quad (29)$$

and

$$\Delta_2 = \sum_{z=0}^{M_{th}} z\binom{z-1}{z-G}\left(1-OP_{D_i}\right)^G\left(OP_{D_i}\right)^{z-G}. \quad (30)$$

From (29) and (30) into (28), we have (27).

IV. PREDICTION OF MAIN OP BASED ON DNN

In this section, we formulate a DNN model for assessing OP. The DNN model serves as a data-driven alternative in cases where the system model is intricate, rendering traditional mathematical derivation approaches challenging to apply.[5] The DNN model will be utilized to both enhance and minimize execution time.

The novelty of our approach lies in the hybrid methodology that combines traditional mathematical derivation with a DNN model. This integration provides a more comprehensive understanding and prediction capability for performance metrics. The DNN enhances the traditional model by learning from data, thus potentially improving accuracy and robustness in complex scenarios. This dual approach represents a significant innovation in handling complex system models. The concern about the applicability of the DNN to other problems is valid. This paper includes a detailed discussion of the adaptability of the DNN framework. Moreover, the DNN approach can be generalized to other complex systems with appropriate modifications. This study provides guidelines for these modifications to ensure the DNN model remains relevant and effective across various applications.

The paper's contribution is twofold: firstly, we offer a rigorous mathematical derivation for performance metrics; secondly, we introduce a DNN model that complements and enhances these derivations. This combined approach offers a robust solution that leverages the strengths of both traditional and modern methodologies. The value of this research lies in its potential to improve performance evaluation in complex systems, thereby making a substantial contribution to the field.

A. THE DNN DESIGN DESCRIPTION

The DNN model employed here is a feed-forward neural network. For a comprehensive view of the DNN's configuration, please refer to Figure 3. The DNN design consists of multiple layers, including an input layer, D_{hid} hidden layers, and an output layer. The functions of each layer in training the DNN model with sample datasets can be summarized as follows [17] and [61].

- The primary function of the input layer is to receive input data, allowing the DNN model to establish connections between system parameters and their corresponding

[5]DNN scheme is similarly applied in [17], [59], and [60]. While we have indeed derived mathematical expressions for performance metrics, the DNN model is introduced to address scenarios where the complexity of the system model may exceed the capabilities of traditional mathematical derivation. The DNN serves as a supplementary tool that can capture intricate patterns and nonlinearities that might be overlooked or too complex to model mathematically.

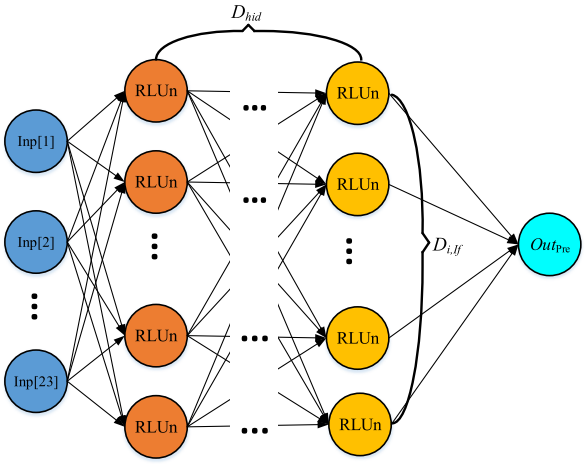

FIGURE 3. DNN model construction for prediction.

OP/ASR/IP (the residual DNN training cases follow a similar process). Neurons in the input layer do not employ activation functions, and their count matches the number of system parameters.

TABLE 2. The system parameters that DNN employs for both testing and training [28], [36], [63], [64].

Inputs	Values	Inputs	Values
τ_s	OP: [35:55] dB; IP: [30:60] dB; ASR: [20:60] dB	d_{r_1}	10 m
$N_1 = N_2$	OP: [25, 30, 50]; IP: 25; ASR: 3	d_{r_2}	30 m
β_1	0.2	τ_{Ja}	10 dB
β_2	0.8	m_h	2
R_1	OP:0.2 (bps/Hz); IP [0.2, 0.3, 0.4] bps/Hz; ASR: None	m_{g_1}	2
R_2	OP: 0.2 bps/Hz; IP: [0.2, 0.3, 0.4] bps/Hz; ASR: None	m_{g_2}	2
η	2	λ_{l_1}	1
δ	OP, ASR: [0.3, 0.5, 0.9]; IP: 0.9	λ_{l_2}	1
G	OP, IP: 10; ASR: 1	λ_{l_e}	1
M_{th}	OP, IP: 10; ASR: 1	d_{J_i}	1
d_s	10 m	d_{J_e}	1

- The hidden layers primarily focus on computing the relationship between input data and output data. Consequently, each connection within these hidden neurons possesses distinct weights and biases to accurately compute this relationship. Furthermore, each hidden neuron integrates a nonlinear activation function to optimize computational efficiency.
- The responsibility of the output layer is to forecast the OP/ASR/IP by incorporating the outcomes from the multiple hidden layers. Consequently, the output layer is composed of a single neuron. Similar to the input layer, the neuron in the output layer does not employ any activation function.

In this model, the primary system parameters are relayed to the server for inclusion as input values, each associated with one of the 23 neurons, as outlined in Table 2. We utilize the output layer, consisting of a single neuron, to generate predictions for OP/ASR/IP. This involves the application of a linear function in conjunction with its associated activation function, as described in [17] and [62]. Moreover, there exist 23 neurons that correspond to the 23 input features (parameters are just weight and bias). In the hidden layers, denoted by layer v with $v = 1, \ldots, D_{hid}$, has $D_{i,If}$ neurons, and the system utilizes the rectified linear unit (RLUn) function as its activation function.

B. GENERATION OF THE DATA SET

The server connected to the BS processes v samples from our dataset, with the relationship between input and output represented as $Data[v] = \left[Inp[v], Out_{D_i}^{G}\right]$, where $Inp[v]$ is a feature vector comprising all the input parameters listed in Table 2. Monte-Carlo simulations utilize the feature vector $Inp[v]$ and subsequently yield an expected secure metric denoted as $Out_{D_i}^{G}$. In summary, we generate a total of 5×10^5 data points and concatenate them to form the dataset. Subsequently, we partition the dataset into three subsets: 80% for training ($\Im_{tra}$), 10% for validation ($\Im_{val}$), and 10% for testing ($\Im_{tes}$).

We use the Mean Square Error (MSE), which is defined as $MSE = \frac{1}{|\Im_{tes}|} \sum_{v=0}^{|\Im_{tes}|-1} (Out_{\Pr e} - Out_{tes})$, to evaluate the performance of the suggested DNN approach. We use Algorithm 1 from [17] and [62] as a guide for the critical steps required for training and evaluating this DNN.

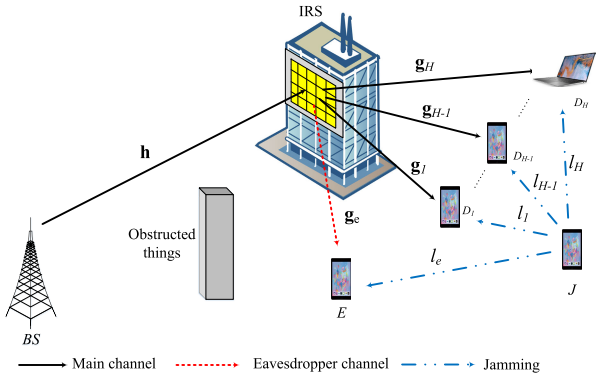

FIGURE 4. The extended scenario involving multiple users.

V. EXTENSION TO MULTI-USER IRS-NOMA SYSTEM

Next, this paper considers the extended IRS-NOMA system with with H users, as presented in Figure 4. We denote the users as $(D_1, D_2, \ldots, D_{H-1}, \ldots, D_H)$, where D_1 is the user closest to BS and IRS, while D_H is the farthest one. In this system, BS sends the packets $c_a[l]$ (denotes the l-th packet of D_a, $a = \{1, 2, \ldots, H\}$) to D_a. Similar to the two-user scheme, BS linearly combines the modulated signals of $c_a[l]$ as $\sum_{a=1}^{H} \sqrt{\beta_a P_s} x_{s_a}[w]$, and then broadcasts the combined signals to the users via RIS, where β_a is used to denote the power allocation coefficients for D_a, subject to constraints

$\beta_1 < \beta_2 < \cdots < \beta_H$ and $\sum_{a=1}^{H} \beta_a = 1$ [65], under the condition that $\mathbf{g}_1\Phi_1\mathbf{h} > \cdots > \mathbf{g}_{H-1}\Phi_{H-1}\mathbf{h} > \cdots > \mathbf{g}_H\Phi_H\mathbf{h}$ [66]. We also assume that the N reflecting elements of the IRS are allocated as follows: $N = N_1 + N_2 + \cdots + N_H$ [41], where N_1 elements are set to steer towards D_1, and the N_2 elements are set to steer towards D_2, ..., and the N_H elements are set to steer towards D_H.

Next, the received signal at D_a, for receiving one encoded packet from BS through IRS, can be expressed as [65]:

$$y_{D_a}^{N} = d_s^{-\frac{\eta}{2}} d_{r_a}^{-\frac{\eta}{2}} \mathbf{g}_a \Phi_a \mathbf{h} \sum_{a=1}^{H} \sqrt{\beta_a P_s} x_{s_a}[w] + d_{J_a}^{-\frac{\eta}{2}} \sqrt{P_{Ja}} l_a x_{Ja}[w] + \sigma_a[w], \quad (31)$$

where d_{r_a} and d_{J_a} are the distances between the IRS and D_a, between the J and D_a, respectively. $\mathbf{g}_a = \left[g_{a,1}, g_{a,2}, \ldots, g_{a,N_a}\right]^T$ represent the complex channel coefficients corresponding to IRS-D_a. The reflection coefficient matrix associated with the BS-IRS-D_a is symbolized by $\Phi_a = \text{diag}\left[\delta_1 e^{j\phi_1^a}, \delta_2 e^{j\phi_2^a}, \ldots, \delta_{N_a} e^{j\phi_{N_a}^a}\right]$, where $\delta_{N_a} \in [0, 1]$ is the amplitude-reflection coefficient, the assumption that $\delta = \delta_1 = \delta_2 = \cdots = \delta_{N_a}$ [42], and $\phi_{n_a}^a \in [0, 2\pi)$ represents the adjustable phase shift variable of the n_a-th element, which can be controlled by the IRS with $n_a = (1, \ldots, N_a)$. Additionally, $\sigma_a[w] \sim CN(0, N_0)$ is the AWGN at D_a, and N_0 is the variance. The Rayleigh fading model characterizes the small-scale fading for both the link from J to D_a, and these are represented by $l_a \sim CN\left(0, \lambda_{l_a}\right)$.

After receiving the combined signals, the user D_a performs SIC to decode its desired data. In particular, D_a first decodes the signal $x_{s_H}[w]$, while treats other signals $x_{s_b}[w], (b = 1, 2, \ldots, H-1)$ as noises [66]. Next, D_a removes $x_{s_H}[w]$ out from the combined signals, and then decodes the next signal $x_{s_{H-1}}[w]$. This process is repeated until D_a can decode its data. It is worth noting that D_H only directly detects its signal without performing SIC, while D_1 must detect all the signals of the remaining users [65]. To more clearly present the SIC operation, we express the SINR at D_d, $(d = 1, 2, \ldots, H-1, H)$ for detecting the signals of D_p, $(p \geq d, p \neq 1)$ as in [65]:

$$\gamma_{D_d}^{x_{sp}} = \frac{d_s^{-\eta} d_{r_d}^{-\eta} \tau_s \beta_p |\mathbf{g}_d \Phi_d \mathbf{h}|^2}{d_s^{-\eta} d_{r_d}^{-\eta} \tau_s |\mathbf{g}_d \Phi_d \mathbf{h}|^2 \sum_{b=1}^{p-1} \beta_b + d_{J_d}^{-\eta} \tau_{Ja} |l_d|^2 + 1}. \quad (32)$$

For the user D_1, the obtained SINR at this node to decode its desired data (after decoding and removing all the signals of the other users) can be expressed as in (3).

We note that D_a can decode its desired signal successfully, it must successfully decode the signals of the users D_b, $b = H, H-1, \ldots, a+1$. Thus, the OP at D_a for one fountain packet can be expressed as [65]:

$$OP_{D_a} = 1 - \Pr\left(\begin{matrix} \gamma_{D_H}^{x_{s_H}} \geq \gamma_H^{th} \cap \gamma_{D_{H-1}}^{x_{s_{H-1}}} \geq \gamma_{H-1}^{th} \\ \cap \cdots \cap \gamma_{D_a}^{x_{s_a}} \geq \gamma_a^{th} \end{matrix}\right), \quad (33)$$

where $\gamma_{D_\Lambda}^{x_{s_\Lambda}} = 2^{R_\Lambda} - 1, \Lambda \in \{H, H-1, \ldots, a\}$, R_Λ is the user D_Λ's target date rate.

Then, similar to (11), the OP at the D_a with G Fountain packets can be written by

$$OP_{D_a}^{G} = \sum_{M_{D_a}=0}^{G-1} \binom{M_{th}}{M_{D_a}} \left(1 - OP_{D_a}\right)^{M_{D_a}} \times \left(OP_{D_a}\right)^{M_{th} - M_{D_a}}. \quad (34)$$

As part of our efforts, the operational principles of the proposed multi-user IRS-NOMA system are presented above. As demonstrated, extending the proposed IRS-NOMA system from two users to multiple users is straightforward. However, due to space limitations, we cannot present the performance analysis of the extended system in this paper. In future research, we will further develop and analyze this extended system.

VI. NUMERICAL RESULTS

Numerical findings illustrating the performance assessment of the network under consideration are presented in this section. Furthermore, the correctness is periodically verified through Monte Carlo simulations. Sim. and Ana. are abbreviations for simulation and analytical, respectively.

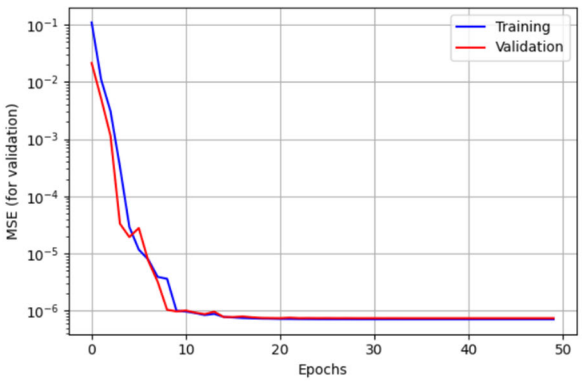

FIGURE 5. The convergence of MSE for OP during the training and validation of DNN with $N_1 = N_2 = 50$.

Figure 5 verifies that the DNN attains the anticipated accuracy as we compare the curves of the training set and validation set. Notably, these two curves closely align with each other. This alignment signifies that the MSE is capable of approaching its lowest error level, and this minimal MSE is achieved after completing 15 epochs.

In Figure 6, we present the OP for two users as a function of τ_s while varying the number of elements N. In the low-τ_s range, the simulation produces precise results for users

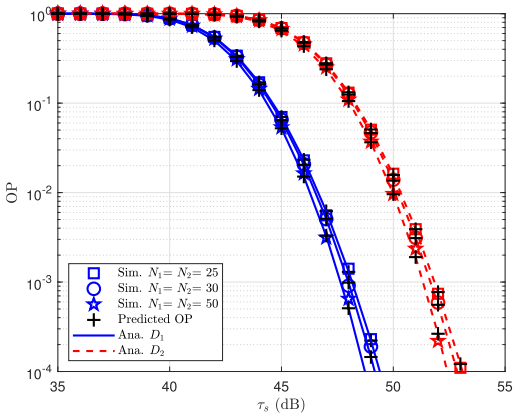

FIGURE 6. OP of D_1, and D_2 versus τ_s, with $N_1 = N_2 = 25, 30, 50$ [35] ($\beta_1 = 0.2$ [63], $R_1 = R_2 = 0.2$ bps/Hz, $\eta = 2$ [63], $\delta = 0.9$ [36], $G = M_{th} = 10$ [28], $d_s = d_{r_1} = 10$ m [64], $d_{r_2} = 30$ m [64], $d_{J_i} = 1$ [63], $\tau_{Ja} = 10$ dB, $m_h = m_{g_1} = m_{g_2} = 2$, $\lambda_{l_1} = \lambda_{l_2} = 1$ [63], [64]).

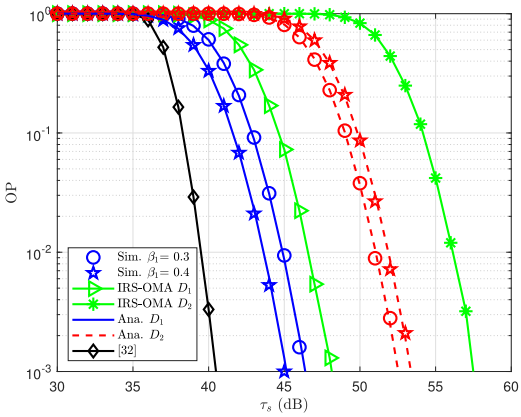

FIGURE 7. OP of D_1, D_2, and the work of [32] versus τ_s, with $\beta_1 = 0.3, 0.4$ ($R_1 = R_2 = 0.2$ bps/Hz [36], $\eta = 2$ [63], $\delta = 0.9$ [36], $G = M_{th} = 10$ [28], $d_s = d_{r_1} = 10$ m [64], $d_{r_2} = 30$ m [64], $d_{J_i} = 1$ [63], $\tau_{Ja} = 10$ dB, $m_h = m_{g_1} = m_{g_2} = 2$ [36], $\lambda_{l_1} = \lambda_{l_2} = 1$ [63], $N_1 = N_2 = 25$ [36]).

D_1 and D_2. Yet, imprecisions manifest in the high-τ_s range attributed to employing channel statistics grounded in the central limit theorem [36] (while we sought to enhance accuracy by augmenting the iteration count, our computer's limitations capped it at a maximum of 10^4 loops). The simulation results for users D_1 and D_2 closely correspond to the numerical results derived from equations (11) and (14) respectively. As the system increases the number of elements N, there is an observable improvement in OP performance. It is important to note that the augmentation of the number of elements in the IRS contributes to this enhancement in OP. However, these factors cannot be ascertained at the *BS* without the assistance of DNN. We can observe that user D_1 exhibits superior OP performance compared to user D_2. The performance gap between these two users, D_1 and D_2, becomes more pronounced as N becomes larger. This discrepancy can be attributed to user D_1 being closer to both the IRS and the *BS* than user D_2. Additionally, the results highlight that as the number of IRS elements increases, not only does the overall OP performance improve, but the relative positioning of the users becomes more critical. This indicates that optimizing the placement and configuration of IRS elements can significantly enhance signal reliability and quality for end-users. Furthermore, the implementation of DNNs to assist in managing the IRS configurations can potentially bridge the performance gap observed between users, ensuring more uniform service quality. These insights are crucial for practical deployments in dense urban areas and large venues, where strategic placement and advanced configuration of IRS elements can make a substantial difference in network performance and user experience.

In Figure 7, we have plotted the OP for two users as a function of τ_s while varying the power allocation values. When comparing the OPs of D_1 and D_2, the simulation results reveal that user D_1 experiences a more favorable scenario due to its proximity to the IRS compared to user D_2. Furthermore, it's important to note that power allocation has a significant influence on OP performance. Furthermore, IRS-NOMA consistently outperforms IRS-OMA for both users D_1 across τ_s ranging from 36 dB to 47 dB and D_2 across τ_s ranging from 44 dB to 53 dB. This superiority of IRS-NOMA highlights the efficiency gains achieved through NOMA, leveraging the unique capabilities of IRS for improved spectral efficiency and user fairness. Additionally, as evident from the comparison, the OP in τ_s range of 36 dB to 45 dB in [32] is lower than that of this paper. This difference can be attributed to the consideration of the jamming device's impact on the system model in this paper, resulting in a higher OP compared to [32]. Figure 8 illustrates the OP for two users as a function of τs while varying the number of M_{th}. It is also noteworthy that the outage performance improves with a higher value of M_{th} because the *BS* has more available time slots to transmit the encoded packets to the D_i. When M_{th} increases from 10 to 15 and from 15 to 20, it means there are more time slots available for transmitting encoded packets within the system. This increase in available time slots allows for a more efficient transmission process from the *BS*. So, the system experiences reduced congestion because more time is allocated for transmitting packets, which leads to a decrease in packet loss and an increase in throughput at D_i [28]. Consequently, this improvement results in a significant enhancement in overall system performance. These findings underscore the importance of dynamic power allocation strategies and the optimization of time slot allocation in IRS-assisted communication systems. By intelligently managing power and time resources, we can maximize the utilization of the available spectrum and enhance system reliability and efficiency, ultimately improving the user experience in diverse wireless communication scenarios.

Transitioning to Figure 9 illustrates the OP diagram relative to the parameter β_1. The results highlight the impact of α_1, showcasing the power allocation's influence on users. As α_1 increases from 0.05 to 0.45, the OP performance improves at D_1, indicating enhanced performance at that location. Conversely, the OP decreases at D_2, demonstrating that increasing power allocation at D_1 comes at the expense of

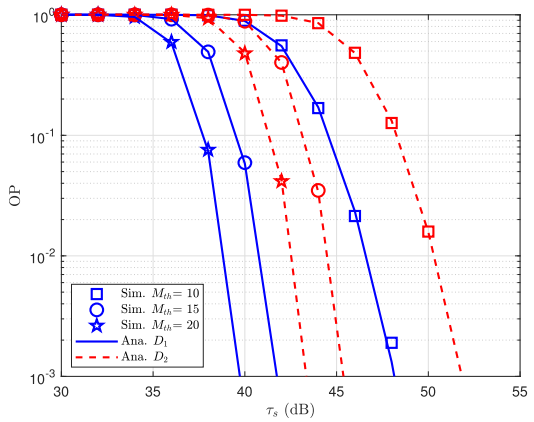

FIGURE 8. OP of D_1, and D_2 versus τ_S, with M_{th} = 10, 15, 20 (β_1 = 0.2 [63], $R_1 = R_2$= 0.2 bps/Hz [36], η = 2 [63], δ = 0.9 [36], G = 10 [28], d_s = d_{r_1} = 10 m [64], d_{r_2} = 30 m [64], d_{J_i} = 1 [63], τ_{Ja} = 10 dB, $m_h = m_{g_1} = m_{g_2}$ = 2 [36], $\lambda_{I_1} = \lambda_{I_2}$ =1 [63], $N_1 = N_2$ = 25 [36]).

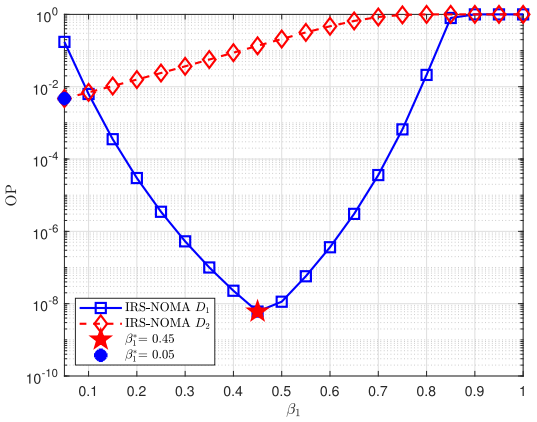

FIGURE 9. OP of D_1, and D_2 versus optimal β_1 (R_1= R_2 = 0.2 bps/Hz [36], η = 2 [63], δ = 0.9 [36], $G = M_{th}$ = 10 [28], $d_s = d_{r_1}$ = 10 m [64], d_{r_2} = 30 m [64], d_{J_i} = 1 [63], τ_{Ja} = 10 dB, $m_h = m_{g_1} = m_{g_2}$ = 2 [36], $\lambda_{I_1} = \lambda_{I_2}$ = 1 [63], $N_1 = N_2$ = 25 [36]).

reduced performance at D_2. This underscores the importance of power allocation and the need for performance balance across different locations. Particularly noteworthy is that for user D_1, optimal performance is achieved at $\beta_1^* = 0.45$, whereas for user D_2, performance peaks at $\beta_1^* = 0.05$.

Figure 10 demonstrates how the system's EE changes concerning τ_s while τ_{Ja} varies. The curve representing the EE of IRS-NOMA networks is plotted based on equation (18). It's apparent that $\tau_{Ja} = 10$ dB stands out as the highest point of system EE among the three cases observed within the τ_s range from 30 dB to 57 dB. However, this heightened EE is constrained specifically in the high range of transmitting τ_s. This limitation arises from the fact that system EE is reliant on outage probability, particularly associated with transmission limitations due to delays. The prominence of τ_{Ja}= 10 dB as the optimal point for maximizing EE underscores the delicate balance between signal strength, interference mitigation, and transmission efficiency in IRS-NOMA networks. This optimal point represents a trade-off between achieving high signal-to-noise ratios for improved communication reliability and minimizing interference from

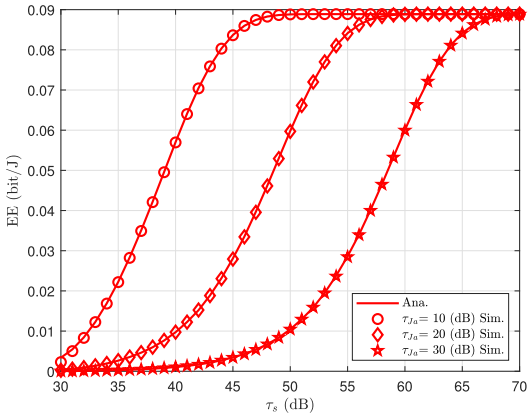

FIGURE 10. System EE versus τ_S, with τ_{Ja} = 10, 20, 30 dB (β_1 = 0.2 [63], $R_1 = R_2$ = 0.2 bps/Hz [36], η = 2 [63], δ = 0.9 [36], $G = M_{th}$ = 1 [28], d_s = d_{r_1} = 10 m [64], d_{r_2} = 30 m [64], d_{J_i} = 1 [63], $m_h = m_{g_1} = m_{g_2}$ = 2 [36], $\lambda_{I_1} = \lambda_{I_2}$ = 1 [63], $N_1 = N_2$ = 25 [36]), ε = 1.2, P_s = 5 dBW, P_{bs} = 2 dBW, P_n (σ) = 10 dBm, P_{D_i} = 10 dBm, P_{J_a} = 10 dBm [52].

external sources, such as jammers. However, it's important to note that this heightened EE is constrained within specific ranges of τ_s, indicating the need for adaptive transmission strategies to optimize EE across varying environmental conditions and network configurations. Understanding the dynamics of EE under different SNR conditions is crucial for designing and deploying efficient wireless communication systems, particularly in scenarios where energy consumption and spectral efficiency are critical factors. By leveraging insights from Figure 10, network operators and system designers can tailor transmission parameters and resource allocation strategies to maximize EE while ensuring reliable and uninterrupted communication services for end-users.

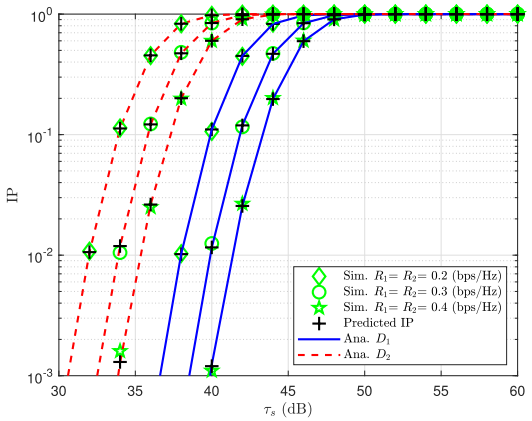

FIGURE 11. IP of D_1, and D_2 versus τ_S, with $R_1 = R_2$ = 0.2, 0.3, 0.4 bps/Hz (β_1 = 0.2 [63], η = 2 [63], δ = 0.9 [36], $G = M_{th}$ = 10 [28], $d_s = d_{r_1} = d_{r_e}$ = 10 m [64], d_{r_2} = 30 m [64], $d_{J_i} = d_{J_e}$ = 1 [63], $\tau_{Ja} = \tau_e = \tau_{Je}$ = 10 dB, $m_h = m_{g_1} = m_{g_2} = m_{ge}$ = 2 [36], $\lambda_{I_1} = \lambda_{I_2} = \lambda_{I_e}$ = 1 [63], N_1= N_2= 25 [36]).

The impacts of the IP of the two users on the τ_s with changing the goal data rate of the two users are shown in Figure 11. It's evident that the IP experiences a notable increase as τ_s increases. This means that higher τ_s results in worse system security. The primary reason for a higher IP is that a higher SNR provides a clearer signal to the

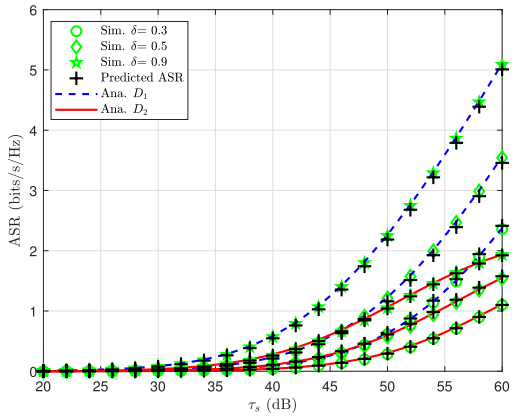

FIGURE 12. ASR of D_1, and D_2 versus τ_s, with $\delta = 0.3, 0.5, 0.9$ ($\beta_1 = 0.2$ [63], $\eta = 2$ [63], $G = M_{th} = 1$ [28], $d_s = d_{r_1} = d_{re} = 10$ m [64], $d_{r_2} = 30$ m [64], $d_{J_i} = d_{J_e} = 1$ [63], $\tau_{Ja} = \tau_e = \tau_{Je} = 10$ dB, $m_h = m_{g_1} = m_{g_2} = m_{ge} = 2$ [36], $\lambda_{I_1} = \lambda_{I_2} = \lambda_{Ie} = 1$ [63], $N_1 = N_2 = 3$ [36], $K = Q = U = 100$ [14]).

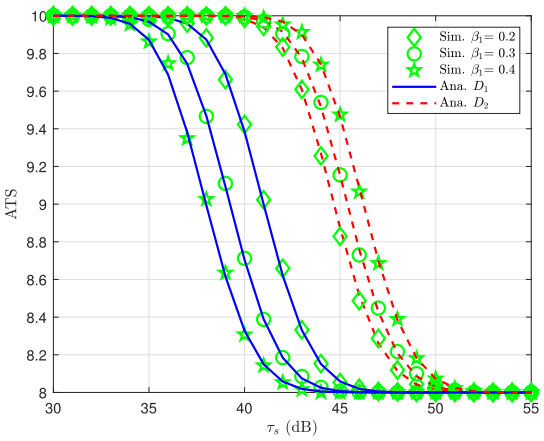

FIGURE 13. ATS of D_1, and D_2 versus τ_s, with $\beta_1 = 0.2, 0.3, 0.4$ ($R_1 = R_2 = 0.2$ bps/Hz, $\eta = 2$ [63], $\delta = 0.9$ [36], $G = 8$ [28], $M_{th} = 10$ [28], $d_s = d_{r_1} = d_{re} = 10$ m [64], $d_{r_2} = 30$ m [64], $d_{J_i} = d_{J_e} = 1$ [63], $\tau_{Ja} = \tau_e = \tau_{Je} = 10$ dB, $m_h = m_{g_1} = m_{g_2} = m_{ge} = 2$ [36], $\lambda_{I_1} = \lambda_{I_2} = \lambda_{Ie} = 1$ [63], [64], $N_1 = N_2 = 25$ [36]).

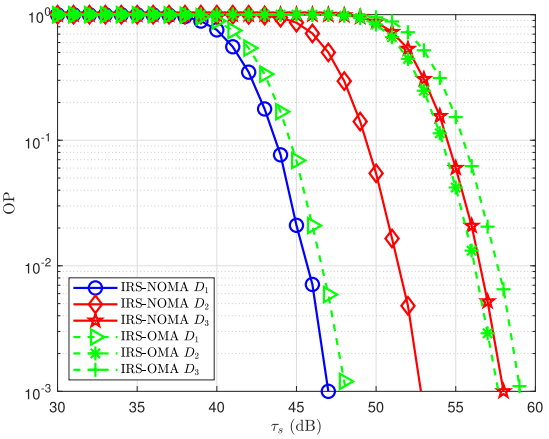

FIGURE 14. Multiple Users Scenario: OP versus τ_s in IRS-NOMA and IRS-OMA systems ($\beta_1 = 0.25$, $\beta_2 = 0.35$, $\beta_3 = 0.4$, $R_1 = R_2 = R_3 = 0.2$ bps/Hz [36], $\eta = 2$ [63], $\delta = 0.9$ [36], $G = M_{th} = 10$ [28], $d_s = d_{r_1} = 10$ m [64], $d_{r_2} = 30$ m [64], $d_{r_3} = 35$ m [64], $d_{J_i} = 1$ [63], $\tau_{Ja} = 10$ dB, $m_h = m_{g_1} = m_{g_2} = m_{g_3} = 2$ [36], $\lambda_{I_1} = \lambda_{I_2} = \lambda_{I_3} = 1$ [63],$N_1 = N_2 = 25$ [36], $H = 3$).

eavesdropper, thereby increasing the likelihood of interception [67]. Please note that, under the given design parameters, the proposed D_1 exhibits a slightly lower intercept probability under the given design parameters than the D_2 model in low-transmission-power regions. Furthermore, it's worth mentioning that the IP for the analyzed schemes also rises as the data rates of both users increase. In Figure 12, ASR curves for users D_1 and D_2 are shown, and the simulated results align with the analytical results obtained from equations (24) and (26). Subsequently, we notice that the ASR of user D_2 also reaches a plateau. Furthermore, the value of δ is relatively high, resulting in an increase in the ASR. Finally, it becomes evident that the DNN-based predictions closely align with the simulation and analysis outcomes for ASR and IP, showcasing the DNN's exceptional predictive prowess. These findings underscore the intricate interplay between system security, data rates, and signal robustness within wireless networks. An in-depth comprehension of the dynamics governing IP and ASR is pivotal for optimizing network security protocols and fortifying communication pathways. Moreover, the corroborative validation of DNN-based prognostications against established methodologies accentuates the potential of machine learning paradigms in fortifying network security and refining performance prognostication within forthcoming wireless communication frameworks.

Figure 13 shows the ATS plotted against the threshold τ_s for different power allocation values. It can be observed that as the transmit power of the *BS* increases, the number of time slots used decreases. This underscores the significance of power allocation, as when more power is allocated to one user, it reduces the number of time slots used for that user but increases the number of time slots used for the other users. Additionally, the trend depicted in Figure 13 offers valuable insights into the dynamics of resource allocation in wireless communication systems. As the transmit power of the *BS* increases, resulting in higher SNRs, the system adapts its time slot allocation strategy accordingly. The observed reduction in the number of time slots used is indicative of a more efficient utilization of resources, as higher SNRs allow for the transmission of data with greater reliability and efficiency in fewer time slots. Moreover, the inverse relationship between power allocation and time slot usage highlights the trade-offs inherent in optimizing system performance. By judiciously allocating power, network operators can prioritize users with higher quality channel conditions, ensuring optimal utilization of available resources while maintaining fairness among users. However, it's crucial to strike a balance between maximizing throughput for individual users and overall system efficiency to meet diverse user requirements and mitigate potential congestion issues. In essence, Figure 13 underscores the intricate interplay between power allocation, time slot utilization, and system performance in wireless communication networks. Understanding these dynamics is essential for designing efficient resource allocation

algorithms and optimizing network operation to meet the evolving demands of modern communication systems.[6]

When considering multiple user scenarios, as shown in Figure 14, user D_3, with a power allocation factor of $\beta_3 = 0.4$, performs worse than the others. This can be explained by the increased interference among all users in a specific group, which becomes a crucial issue when the number of users is greater than two. Moreover, as noted in previous figures, the performance of the IRS-NOMA system consistently surpasses that of the IRS-OMA system as τ_s increases from 40 dB to 59 dB.

VII. CONCLUSION

In this research paper, we analyzed the performance aspects of IRS-based NOMA networks, with a particular focus on security implications. To enhance secure communication, we introduced techniques such as FC-based and cooperative jamming. Additionally, we leveraged DNN capabilities to incorporate intelligent functionality within the base station of the IRS-NOMA system, addressing specific security needs and improving the performance of two legitimate users. We validated our theoretical expressions for various security metrics, including ASR and IP, along with performance metrics like OP, EE, and ATS, through extensive simulations. Our analysis of the OP demonstrated that IRS-NOMA consistently outperforms IRS-OMA in terms of outage behavior. Notably, our findings highlighted the critical roles of several factors in enhancing the security and performance of IRS-NOMA systems, including the number of reflecting elements at the IRS, the power allocation coefficient, the upper limit encountered by encoded packets, the power of the jamming device, the user data rate, and the amplitude-reflection coefficient. In the future, we plan to integrate Relay NOMA with adaptable intelligent surfaces and explore the IRS-NOMA system model with multiple users to further enhance system performance metrics.

APPENDIX A PROOF OF THE THEOREM 1

Based on [36] and [41], in the *BS*-IRS-D_i link and *BS*-IRS-E link, our goal is to optimize the channel quality for D_i and E through adjustments in the IRS parameters. This entails maximizing $\left|\mathbf{g}_q \Phi_q \mathbf{h}\right| = \left|\sum_{n=1}^{c} \delta h_n g_{q,n} e^{j\phi_n^q}\right|$, $q \in \{1, 2, e\}$, $c \in \{N_1, N_2\}$, where h_n and $g_{q,n}$ represent the nth elements of $\mathbf{h}$ and $\mathbf{g}_q$, respectively. Achieving this optimization requires intelligent manipulation of the phase-shift variable ϕ_n^q for each element, with all $h_n g_{q,n} e^{j\phi_n^q}$ phases set to be identical. Consequently, there isn't a unique solution for ϕ_n^q, $(n = 1, \ldots, c)$, and the comprehensive solution is provided by $\phi_n^q = \bar{\phi} - \arg\left(h_n g_{q,n}\right)$, with $\bar{\phi}$ as an arbitrary constant within the range of $[0, 2\pi)$. Upon implementing the optimal $\{\phi_n^q\}$, we obtain: $\left|\mathbf{g}_q \Phi_q \mathbf{h}\right|^2 = \delta^2 \left|\sum_{n=1}^{c} h_n g_{q,n}\right|^2$ [36].

The PDF and CDF of $Y_q = \frac{\left(\sum_{n=1}^{c} |h_n||g_{q,n}|\right)^2}{c(1-\varepsilon_q)}$ are expressed as follows [36]:

$$f_{Y_q}(y_q) = \frac{\lambda_q^{1/4}}{2} \exp\left(-\frac{y_q + \lambda_q}{2}\right) y_q^{-1/4} I_{-1/2}\left(\sqrt{\lambda_q y_q}\right) = \exp\left(-\frac{y_q + \lambda_q}{2}\right) \sum_{m=0}^{\infty} \frac{\lambda_q^m y_q^{m-1/2}}{m! 2^{2m+1/2} \Gamma(m + 1/2)}, \quad (35)$$

and

$$F_{Y_q}(y_q) = 1 - Q_{1/2}\left(\sqrt{\lambda_q}, \sqrt{y_q}\right) = \exp\left(-\frac{\lambda_q}{2}\right) \sum_{m=0}^{\infty} \frac{\lambda_q^m \gamma\left(m + 1/2, y_q/2\right)}{m! 2^m \Gamma(m + 1/2)}, \quad (36)$$

where

$$\varepsilon_q = \frac{1}{m_h m_{g_q}} \left(\frac{\Gamma(m_h + 1/2)}{\Gamma(m_h)}\right)^2 \left(\frac{\Gamma\left(m_{g_q} + 1/2\right)}{\Gamma\left(m_{g_q}\right)}\right)^2,$$
$$\lambda_q = \frac{c\varepsilon_q}{1 - \varepsilon_q}.$$

As the number of reflecting elements N becomes substantial, Y_q tends to conform to a noncentral chi-square distribution like $Y_q \sim Y_q^2(\lambda_q)$. $I_y(.)$ represents the modified Bessel function of the first kind, $Q_y(.)$ stands for the Marcum Q-function, $\Gamma(.)$ denotes the gamma function, and $\gamma(.,.)$ is the lower incomplete gamma function.

The PDF and CDF of $\left|l_q\right|^2$ can be written as [69]

$$f_{|l_q|^2}(x) = \frac{1}{\varphi_Y} e^{-\frac{x}{\lambda_{l_q}}}, \quad (37)$$

$$F_{|l_q|^2}(x) = 1 - e^{-\frac{x}{\lambda_{l_q}}}. \quad (38)$$

From (8), we can rewrite the OP at D_1 as

$$OP_{D_1} = \Pr\left(|l_1|^2 > \frac{\tau_s\left(\sum_{n=1}^{N_1} |h_n|\,|g_{1,n}|\right)^2 - \omega}{\omega d_1^{-\eta} \tau_{Ja}}\right) = \int_0^{\infty} \left(1 - F_{|l_1|^2}\left(\frac{\tau_s x - \omega}{\omega d_1^{-\eta} \tau_{Ja}}\right)\right) f_{\left(\sum_{n=1}^{N_1} |h_n||g_{1,n}|\right)^2}(x)\, dx, \quad (39)$$

where $\xi_1 = \frac{d_s^{-\eta} d_{r_1}^{-\eta} \delta^2}{N_1(1-\varepsilon_1)}$, $\omega = \max\left(\frac{\gamma_2^{th}}{(\beta_2 - \gamma_2^{th}\beta_1)\xi_1}, \frac{\gamma_1^{th}}{\xi_1 \beta_1}\right)$. Based on (35) and (38), OP_{D_1} can be calculated as

$$OP_{D_1} = \exp\left(\frac{\omega}{\omega d_1^{-\eta} \tau_{Ja} \lambda_{l_1}} - \frac{\lambda_1}{2}\right) \sum_{m=0}^{\infty} \frac{\lambda_1^m}{m! 2^{2m+1/2} \Gamma(m + 1/2)}$$

[6] Our findings can serve as valuable guidelines for brainstorming new features in real-world applications. For instance, a recent study [68] developed a prototype of a IRS as a proof of concept, thoroughly evaluating its potential benefits in practical wireless communication environments. Initially, a 160-element reconfigurable surface was designed, manufactured, and tested to demonstrate how this IRS technique mitigates path loss and extends coverage in real-world outdoor communication scenarios.

$$\times \int_0^{\infty} x^{m+1/2-1} \exp\left(-\left(\frac{\tau_s}{\omega d_{J_1}^{-\eta}\tau_{Ja}\lambda_{l_1}}+\frac{1}{2}\right)x\right)dx. \quad (40)$$

With the use of the [56, Eq. (3.381.4)] the equation (9) can be obtained from the (40) expression. The proof is finished.

APPENDIX B PROOF OF THE THEOREM 3

From (23), Ψ_1 can be written by

$$\Psi_1 = \frac{1}{\ln 2}\int_0^{\infty} \frac{1-F_{\gamma_{D_1}^{x_1}}(x)}{1+x}dx. \quad (41)$$

Next, $F_{\gamma_{D_1}^{x_1}}(x)$ can be derived as

$$F_{\gamma_{D_1}^{x_1}}(x) = 1-$$
$$\Pr\left(\left(\sum_{n=1}^{N_1}|h_n|\,|g_{1,n}|\right)^2 > \frac{x\left(d_{J_1}^{-\eta}\tau_{Ja}|l_1|^2+1\right)}{\xi_1\beta_1\tau_s}\right)$$
$$= 1-\int_0^{\infty}\left(1-F_{\left(\sum_{n=1}^{N_1}|h_n||g_{1,n}|\right)^2}\left(\frac{x\left(d_{J_1}^{-\eta}\tau_{Ja}y+1\right)}{\xi_1\beta_1\tau_s}\right)\right)$$
$$\times f_{|l_1|^2}(y)\,dy$$
$$= 1-\frac{\exp\left(-\frac{\lambda_1}{2}\right)}{\lambda_{l_1}}\sum_{m=0}^{\infty}\frac{\lambda_1^m}{m!2^m\Gamma(m+1/2)}\times$$
$$\int_0^{\infty}\Gamma\left(m+1/2,\frac{x\left(d_{J_1}^{-\eta}\tau_{Ja}y+1\right)}{2\xi_1\beta_1\tau_s}\right)\exp\left(-\frac{y}{\lambda_{l_1}}\right)dy. \quad (42)$$

Since it is challenging to get an exact formula for $F_{\gamma_{D_1}^{x_1}}(x)$ from (42), we suppose that when Q is big and we apply Gaussian-Chebyshev quadrature [56], we have

$$F_{\gamma_{D_1}^{x_1}}(x) = 1-\frac{\exp\left(-\frac{\lambda_1}{2}\right)}{\lambda_{l_1}}\sum_{m=0}^{\infty}\frac{\lambda_1^m}{m!2^m\Gamma(m+1/2)}$$
$$\times\int_0^{Q}\Gamma\left(m+1/2,\frac{x\left(d_{J_1}^{-\eta}\tau_{Ja}y+1\right)}{2\xi_1\beta_1\tau_s}\right)\exp\left(-\frac{y}{\lambda_{l_1}}\right)dy$$
$$= 1-\sum_{m=0}^{\infty}\sum_{k=1}^{K}\frac{\lambda_1^m\sqrt{1-t_k^2}}{m!2^m\Gamma(m+1/2)}\frac{Q\pi\exp\left(-\frac{\lambda_1}{2}\right)}{2K\lambda_{l_1}}$$
$$\times\Gamma\left(m+\frac{1}{2},\frac{x\left(d_{J_1}^{-\eta}\tau_{Ja}\Xi+1\right)}{2\xi_1\beta_1\tau_s}\right)\exp\left(-\frac{\Xi}{\lambda_{l_1}}\right), \quad (43)$$

where $\Xi = \frac{Qt_k+Q}{2}$, $t_k = \cos\left[\frac{(2k-1)\pi}{2K}\right]$, K is a trade-off parameter for accuracy and complexity.

From (43) into (41), Ψ_1 can formulate

$$\Psi_1 = \frac{1}{\ln 2}\sum_{m=0}^{\infty}\sum_{k=1}^{K}\frac{\lambda_1^m\sqrt{1-t_k^2}}{m!2^m\Gamma(m+1/2)}\frac{Q\pi\exp\left(-\frac{\lambda_1}{2}-\frac{\Xi}{\lambda_{l_1}}\right)}{2K\lambda_{l_1}}$$
$$\times\int_0^{\infty}(1+x)^{-1}G_{1,2}^{2,0}\left(\begin{matrix}1\\ m+\frac{1}{2},0\end{matrix}\middle|\frac{x\left(d_{J_1}^{-\eta}\tau_{Ja}\Xi+1\right)}{2\xi_1\beta_1\tau_s}\right)dx, \quad (44)$$

where $G_{p,1}^{m,n}(.)$ is the Meijer G-function [56, Eq. (9.301)]. Additionally, we use equality [70, Eq. (2.6)] as $\Gamma(S,Ix) = G_{1,2}^{2,0}\left(\begin{matrix}1\\ S,0\end{matrix}\middle|Ix\right)$.

Utilizing the additional assistance provided by equation [56, Eq. (7.811.5)], we can express Ψ_1 as

$$\Psi_1 = \frac{1}{\ln 2}\sum_{m=0}^{\infty}\sum_{k=1}^{K}\frac{\lambda_1^m\sqrt{1-t_k^2}}{m!2^m\Gamma(m+1/2)}\frac{Q\pi\exp\left(-\frac{\lambda_1}{2}-\frac{\Xi}{\lambda_{l_1}}\right)}{2K\lambda_{l_1}}$$
$$\times G_{2,3}^{3,1}\left(\begin{matrix}0,1\\ 0,m+\frac{1}{2},0\end{matrix}\middle|\frac{\left(d_{J_1}^{-\eta}\tau_{Ja}\Xi+1\right)}{2\xi_1\beta_1\tau_s}\right). \quad (45)$$

From (23), Ψ_2 can be written by

$$\Psi_2 = \frac{1}{\ln 2}\int_0^{\infty}\frac{1-F_{\gamma_E^{x_1}}(x)}{1+x}dx. \quad (46)$$

Ψ_2 is calculated similarly to Ψ_1, for ease of presentation, we omit the derivation steps, and express Ψ_2 as below:

$$\Psi_2 = \frac{1}{\ln 2}\sum_{m=0}^{\infty}\sum_{k=1}^{K}\frac{\lambda_e^m\sqrt{1-t_k^2}}{m!2^m\Gamma(m+1/2)}$$
$$\times\frac{Q\pi\exp\left(-\frac{\lambda_e}{2}-\frac{\Xi}{\lambda_{l_e}}\right)}{2K\lambda_{l_e}}$$
$$\times G_{2,3}^{3,1}\left(\begin{matrix}0,1\\ 0,m+\frac{1}{2},0\end{matrix}\middle|\frac{\left(d_{J_e}^{-\eta}\tau_{Je}\Xi+1\right)}{2\xi_e\beta_1\tau_e}\right). \quad (47)$$

We may extract expression (24), which is obtained by converting equations (45) and (47) into (23). The proof is finished.

APPENDIX C PROOF OF THE THEOREM 4

From (25), Ψ_3 can be written by

$$\Psi_3 = \frac{1}{\ln 2}\int_0^{\infty}\frac{1-F_{\gamma_{D_2}^{x_2}}(x)}{1+x}dx. \quad (48)$$

Based on equations (42) and (47), $F_{\gamma_{D_2}^{x_2}}(x)$ can be expressed as follows:

$$F_{\gamma_{D_2}^{x_2}}(x)$$
$$= 1-\Pr\left(\left(\sum_{n=1}^{N_2}|h_n|\,|g_{2,n}|\right)^2 > \frac{x\left(d_{J_2}^{-\eta}\tau_{Ja}|l_2|^2+1\right)}{(\beta_2-x\beta_1)\,\xi_2\tau_s}\right)$$
$$= 1-\int_0^{\infty}\left(1-F_{\left(\sum_{n=1}^{N_2}|h_n||g_{2,n}|\right)^2}\left(\frac{x\left(d_{J_2}^{-\eta}\tau_{Ja}y+1\right)}{(\beta_2-x\beta_1)\,\xi_2\tau_s}\right)\right)$$

$$\times f_{|l_2|^2}(y)\,dy$$
$$= 1 - \frac{\exp\left(-\frac{\lambda_2}{2}\right)}{\lambda_{l_2}} \sum_{m=0}^{\infty} \frac{\lambda_2^m}{m!2^m\Gamma(m+1/2)} \times \int_0^{\infty} \Gamma\left(m+1/2, \frac{x\left(d_{J_2}^{-\eta}\tau_{Ja}y+1\right)}{2\left(\beta_2 - x\beta_1\right)\xi_2\tau_s}\right) \exp\left(-\frac{y}{\lambda_{l_2}}\right) dy. \tag{49}$$

Similar to (43), since obtaining an exact closed-form formula for $F_{\gamma_{D_2}^{x_2}}(x)$ from (49) is difficult, we assume that when Q is large and we use Gaussian-Chebyshev quadrature [56], we have

$$F_{\gamma_{D_2}^{x_2}}(x) = 1 - \frac{\exp\left(-\frac{\lambda_2}{2}\right)}{\lambda_{l_2}} \sum_{m=0}^{\infty} \frac{\lambda_2^m}{m!2^m\Gamma(m+1/2)} \times \int_0^{Q} \Gamma\left(m+1/2, \frac{x\left(d_{J_2}^{-\eta}\tau_{Ja}y+1\right)}{2\left(\beta_2 - x\beta_1\right)\xi_2\tau_s}\right) \exp\left(-\frac{y}{\lambda_{l_2}}\right) dy$$
$$= 1 - \sum_{m=0}^{\infty}\sum_{k=1}^{K} \frac{\lambda_2^m\sqrt{1-t_k^2}}{m!2^m\Gamma(m+1/2)} \frac{Q\pi\exp\left(-\frac{\lambda_2}{2}\right)}{2K\lambda_{l_2}} \times \Gamma\left(m+\frac{1}{2}, \frac{x\left(d_{J_2}^{-\eta}\tau_{Ja}\Xi+1\right)}{2\left(\beta_2 - x\beta_1\right)\xi_2\tau_s}\right) \exp\left(-\frac{\Xi}{\lambda_{l_2}}\right). \tag{50}$$

Similar to (44), we employ the equality [70, Eq. (2.6)], and in addition, by utilizing Gaussian-Chebyshev quadrature [56], we obtain:

$$\Psi_3 = \frac{1}{\ln 2}\sum_{m=0}^{\infty}\sum_{k=1}^{K} \frac{\lambda_2^m\sqrt{1-t_k^2}}{m!2^m\Gamma(m+1/2)} \frac{Q\pi\exp\left(-\frac{\lambda_2}{2}-\frac{\Xi}{\lambda_{l_2}}\right)}{2K\lambda_{l_2}} \times \int_0^{\frac{\beta_2}{\beta_1}} (1+x)^{-1}\Gamma\left(m+\frac{1}{2}, \frac{x\left(d_{J_2}^{-\eta}\tau_{Ja}\Xi+1\right)}{2\left(\beta_2-x\beta_1\right)\xi_2\tau_s}\right) dx$$
$$= \frac{1}{\ln 2}\sum_{m=0}^{\infty}\sum_{k=1}^{K}\sum_{u=1}^{U} \frac{\lambda_2^m\sqrt{1-t_k^2}\sqrt{1-z_u^2}}{m!2^m\Gamma(m+1/2)} \times \frac{\beta_2 Q\pi\pi\exp\left(-\frac{\lambda_2}{2}-\frac{\Xi}{\lambda_{l_2}}\right)}{4\beta_1 KU\lambda_{l_2}(1+\Theta)} \times \Gamma\left(m+\frac{1}{2}, \frac{\Theta\left(d_{J_2}^{-\eta}\tau_{Ja}\Xi+1\right)}{2\left(\beta_2-\Theta\beta_1\right)\xi_2\tau_s}\right), \tag{51}$$

where $z_u = \cos\left[\frac{(2u-1)\pi}{2U}\right]$, $\Theta = \frac{\beta_2 z_u+\beta_2}{2\beta_1}$, U is a trade-off parameter for accuracy and complexity.

The calculation procedure for Ψ_4 closely resembles that of Ψ_2. Therefore, as we proceed through the calculation steps, the expression of Ψ_4 can be provided below:

$$\Psi_4 = \frac{1}{\ln 2}\sum_{m=0}^{\infty}\sum_{k=1}^{K} \frac{\lambda_e^m\sqrt{1-t_k^2}}{m!2^m\Gamma(m+1/2)} \frac{Q\pi\exp\left(-\frac{\lambda_e}{2}-\frac{\Xi}{\lambda_{l_e}}\right)}{2K\lambda_{l_e}} \times G_{2,3}^{3,1}\left(\begin{matrix}0,1\\0,m+\frac{1}{2},0\end{matrix}\middle|\frac{\left(d_{J_e}^{-\eta}\tau_{Je}\Xi+1\right)}{2\xi_e\beta_2\tau_e}\right). \tag{52}$$

Expression (26) can be derived by transforming equations (51) and (52) into (25). This concludes the proof.

REFERENCES

[1] Z. Zhang, L. Dai, X. Chen, C. Liu, F. Yang, R. Schober, and H. V. Poor, "Active RIS vs. passive RIS: Which will prevail in 6G?" *IEEE Trans. Commun.*, vol. 71, no. 3, pp. 1707–1725, Mar. 2023.

[2] B. Zheng, C. You, W. Mei, and R. Zhang, "A survey on channel estimation and practical passive beamforming design for intelligent reflecting surface aided wireless communications," *IEEE Commun. Surveys Tuts.*, vol. 24, no. 2, pp. 1035–1071, 2nd Quart., 2022.

[3] T. N. Nguyen, N. N. Thang, B. C. Nguyen, T. M. Hoang, and P. T. Tran, "Intelligent-reflecting-surface-aided bidirectional full-duplex communication system with imperfect self-interference cancellation and hardware impairments," *IEEE Syst. J.*, vol. 17, no. 1, pp. 1352–1362, Mar. 2023.

[4] P. T. Tran, B. C. Nguyen, T. M. Hoang, and T. N. Nguyen, "On performance of low-power wide-area networks with the combining of reconfigurable intelligent surfaces and relay," *IEEE Trans. Mobile Comput.*, vol. 22, no. 10, pp. 6086–6096, Oct. 2023.

[5] M. Elhattab, M. A. Arfaoui, C. Assi, and A. Ghrayeb, "RIS-assisted joint transmission in a two-cell downlink NOMA cellular system," *IEEE J. Sel. Areas Commun.*, vol. 40, no. 4, pp. 1270–1286, Apr. 2022.

[6] A. Chauhan, S. Ghosh, and A. Jaiswal, "RIS partition-assisted non-orthogonal multiple access (NOMA) and quadrature-NOMA with imperfect SIC," *IEEE Trans. Wireless Commun.*, vol. 22, no. 7, pp. 4371–4386, Jul. 2023.

[7] S. V. Hum and J. Perruisseau-Carrier, "Reconfigurable reflectarrays and array lenses for dynamic antenna beam control: A review," *IEEE Trans. Antennas Propag.*, vol. 62, no. 1, pp. 183–198, Jan. 2014.

[8] C. Huang, G. C. Alexandropoulos, A. Zappone, M. Debbah, and C. Yuen, "Energy efficient multi-user MISO communication using low resolution large intelligent surfaces," in *Proc. IEEE GLOBECOM Workshops (GC Wkshps)*, Dec. 2018, pp. 1–6.

[9] Ö. Özdogan, E. Björnson, and E. G. Larsson, "Intelligent reflecting surfaces: Physics, propagation, and pathloss modeling," *IEEE Wireless Commun. Lett.*, vol. 9, no. 5, pp. 581–585, May 2020.

[10] S. A. Tegos, D. Tyrovolas, P. D. Diamantoulakis, C. K. Liaskos, and G. K. Karagiannidis, "On the distribution of the sum of double-Nakagami-*m* random vectors and application in randomly reconfigurable surfaces," *IEEE Trans. Veh. Technol.*, vol. 71, no. 7, pp. 7297–7307, Jul. 2022.

[11] D. Tyrovolas, P.-V. Mekikis, S. A. Tegos, P. D. Diamantoulakis, C. K. Liaskos, and G. K. Karagiannidis, "On the performance of HARQ in IoT networking with UAV-mounted reconfigurable intelligent surfaces," in *Proc. IEEE 95th Veh. Technol. Conf. (VTC-Spring)*, Jun. 2022, pp. 1–5.

[12] Y. Ni, Y. Liu, J. Wang, Q. Wang, H. Zhao, and H. Zhu, "Performance analysis for RIS-assisted D2D communication under Nakagami-*m* fading," *IEEE Trans. Veh. Technol.*, vol. 70, no. 6, pp. 5865–5879, Jun. 2021.

[13] P. M. Quang, N. T. Kien, T. T. Duy, N. H. An, N. T. Tung, and A.-V. Le, "Performance evaluation of reconfigurable intelligent surface aided multi-hop relaying schemes with short packet communication," *Adv. Electr. Electron. Eng.*, vol. 22, no. 1, pp. 97–106, 2024.

[14] M.-S. Van Nguyen, D.-T. Do, A. Vahid, S. Muhaidat, and D. Sicker, "Enhancing NOMA backscatter IoT communications with RIS," *IEEE Internet Things J.*, vol. 11, no. 4, pp. 5604–5622, Feb. 2024.

[15] M.-S. Van Nguyen, D.-T. Do, S. Al-Rubaye, S. Mumtaz, A. Al-Dulaimi, and O. A. Dobre, "Exploiting impacts of antenna selection and energy harvesting for massive network connectivity," *IEEE Trans. Commun.*, vol. 69, no. 11, pp. 7587–7602, Nov. 2021.

[16] T. L. Nguyen, T.-L. Nguyen, V. V. Nguyen, and T. T. Phu, "Outage performance of full-duplex unmanned aerial vehicle-aided cooperative non-orthogonal multiple access," *Adv. Electr. Electron. Eng.*, vol. 21, no. 1, pp. 1–8, May 2023.
[17] K. Shim, T. N. Do, T.-V. Nguyen, D. B. da Costa, and B. An, "Enhancing PHY-security of FD-enabled NOMA systems using jamming and user selection: Performance analysis and DNN evaluation," *IEEE Internet Things J.*, vol. 8, no. 24, pp. 17476–17494, Dec. 2021.
[18] V. Phan, T. Nguyen, T. Phu, and V. Nguyen, "Reliability-security in wireless-powered cooperative network with friendly jammer," *Adv. Electr. Electron. Eng.*, vol. 20, no. 4, pp. 584–591, 2023.
[19] V.-L. Dao, E. Uhlemann, and S. Girs, "Dealing with jamming attacks in uplink pairwise NOMA using outage analysis, smart relaying, and redundant transmissions," *IEEE Open J. Commun. Soc.*, vol. 5, pp. 112–126, 2024.
[20] T. N. Nguyen, D.-H. Tran, T. V. Chien, V.-D. Phan, M. Voznak, P. T. Tin, S. Chatzinotas, D. W. K. Ng, and H. V. Poor, "Security–reliability tradeoff analysis for SWIPT- and AF-based IoT networks with friendly jammers," *IEEE Internet Things J.*, vol. 9, no. 21, pp. 21662–21675, Nov. 2022.
[21] P. M. Nam, H. D. Hung, T. T. Duy, and L. T. Thuong, "Security-reliability trade-off of MIMO TAS/SC networks using harvest-to-jam cooperative jamming methods with random jammer location," *ICT Exp.*, vol. 9, no. 1, pp. 63–68, 2023.
[22] B. V. Minh, M. Tran, V. D. Phan, and N. Hieu, "D2D communication network with the assistance of power beacon under the impact of co-channel interferences and eavesdropper: Performance analysis," *Adv. Electr. Electron. Eng.*, vol. 21, no. 4, pp. 351–359, Dec. 2023.
[23] Z. Zheng, L. Yuan, and F. Fang, "Performance analysis of fountain coded non-orthogonal multiple access with finite blocklength," *IEEE Wireless Commun. Lett.*, vol. 10, no. 8, pp. 1752–1756, Aug. 2021.
[24] L. Yuan, K. J. Kim, and J. Zhang, "Cross-layer design for fountain coded non-orthogonal multiple access transmission," in *Proc. IEEE Int. Conf. Commun. (ICC)*, May 2019, pp. 1–5.
[25] N. P. Douglass, J. Langel, W. J. Moore, L. Ng, R. M. Dudukovich, and S. Mal-Sarkar, "Application of fountain code to high-rate delay tolerant networks," *IEEE Access*, vol. 11, pp. 100845–100855, 2023.
[26] J. Yue, Z. Lin, and B. Vucetic, "Distributed fountain codes with adaptive unequal error protection in wireless relay networks," *IEEE Trans. Wireless Commun.*, vol. 13, no. 8, pp. 4220–4231, Aug. 2014.
[27] H. D. T. Nguyen, L.-N. Tran, and E.-K. Hong, "On transmission efficiency for wireless broadcast using network coding and fountain codes," *IEEE Commun. Lett.*, vol. 15, no. 5, pp. 569–571, May 2011.
[28] L.-T. Tu, T. N. Nguyen, T. T. Duy, P. T. Tran, M. Voznak, and A. I. Aravanis, "Broadcasting in cognitive radio networks: A fountain codes approach," *IEEE Trans. Veh. Technol.*, vol. 71, no. 10, pp. 11289–11294, Oct. 2022.
[29] A. Ali, K. S. Kwak, N. H. Tran, Z. Han, D. Niyato, F. Zeshan, M. T. Gul, and D. Y. Suh, "RaptorQ-based efficient multimedia transmission over cooperative cellular cognitive radio networks," *IEEE Trans. Veh. Technol.*, vol. 67, no. 8, pp. 7275–7289, Aug. 2018.
[30] C. Berger, S. Zhou, Y. Wen, P. Willett, and K. Pattipati, "Optimizing joint erasure- and error-correction coding for wireless packet transmissions," *IEEE Trans. Wireless Commun.*, vol. 7, no. 11, pp. 4586–4595, Nov. 2008.
[31] V. Sgardoni and A. R. Nix, "Raptor code-aware link adaptation for spectrally efficient unicast video streaming over mobile broadband networks," *IEEE Trans. Mobile Comput.*, vol. 14, no. 2, pp. 401–415, Feb. 2015.
[32] S.-P. Le, H.-N. Nguyen, N.-T. Nguyen, C. H. Van, A.-T. Le, and M. Voznak, "Physical layer security analysis of IRS-based downlink and uplink NOMA networks," *EURASIP J. Wireless Commun. Netw.*, vol. 2023, no. 1, p. 105, Oct. 2023.
[33] W. Li, Q. Du, L. Sun, P. Ren, and Y. Wang, "Security enhanced via dynamic fountain code design for wireless delivery," in *Proc. IEEE Wireless Commun. Netw. Conf.*, Apr. 2016, pp. 1–6.
[34] I. Trigui, W. Ajib, and W.-P. Zhu, "Secrecy outage probability and average rate of RIS-aided communications using quantized phases," *IEEE Commun. Lett.*, vol. 25, no. 6, pp. 1820–1824, Jun. 2021.
[35] L. Yang, J. Yang, W. Xie, M. O. Hasna, T. Tsiftsis, and M. D. Renzo, "Secrecy performance analysis of RIS-aided wireless communication systems," *IEEE Trans. Veh. Technol.*, vol. 69, no. 10, pp. 12296–12300, Oct. 2020.
[36] Y. Cheng, K. H. Li, Y. Liu, K. C. Teh, and H. V. Poor, "Downlink and uplink intelligent reflecting surface aided networks: NOMA and OMA," *IEEE Trans. Wireless Commun.*, vol. 20, no. 6, pp. 3988–4000, Jun. 2021.
[37] S. Khan and S. Y. Shin, "Deep learning aided transmit power estimation in mobile communication system," *IEEE Commun. Lett.*, vol. 23, no. 8, pp. 1405–1408, Aug. 2019.
[38] C. Huang, G. C. Alexandropoulos, C. Yuen, and M. Debbah, "Indoor signal focusing with deep learning designed reconfigurable intelligent surfaces," in *Proc. IEEE 20th Int. Workshop Signal Process. Adv. Wireless Commun. (SPAWC)*, Jul. 2019, pp. 1–5.
[39] Z. Ding, M. Peng, and H. V. Poor, "Cooperative non-orthogonal multiple access in 5G systems," *IEEE Commun. Lett.*, vol. 19, no. 8, pp. 1462–1465, Aug. 2015.
[40] H. Niu, M. Iwai, K. Sezaki, L. Sun, and Q. Du, "Exploiting fountain codes for secure wireless delivery," *IEEE Commun. Lett.*, vol. 18, no. 5, pp. 777–780, May 2014.
[41] X. Li, J. Zhang, C. Han, W. Hao, M. Zeng, Z. Zhu, and H. Wang, "Reliability and security of CR-STAR-RIS-NOMA assisted IoT networks," *IEEE Internet Things J.*, early access, Dec. 7, 2023, doi: 10.1109/JIOT.2023.3340371.
[42] S. Li, L. Bariah, S. Muhaidat, A. Wang, and J. Liang, "Outage analysis of NOMA-enabled backscatter communications with intelligent reflecting surfaces," *IEEE Internet Things J.*, vol. 9, no. 16, pp. 15390–15400, Aug. 2022.
[43] D. Selimis, K. P. Peppas, G. C. Alexandropoulos, and F. I. Lazarakis, "On the performance analysis of RIS-empowered communications over Nakagami-*m* fading," *IEEE Commun. Lett.*, vol. 25, no. 7, pp. 2191–2195, Jul. 2021.
[44] Z. Ding and H. Vincent Poor, "A simple design of IRS-NOMA transmission," *IEEE Commun. Lett.*, vol. 24, no. 5, pp. 1119–1123, May 2020.
[45] A. Souzani, M. A. Pourmina, P. Azmi, and M. Naser-Moghadasi, "Physical layer security enhancement via IRS based on PD-NOMA and cooperative jamming," *IEEE Access*, vol. 11, pp. 65956–65967, 2023.
[46] K. Cao, H. Ding, B. Wang, L. Lv, J. Tian, Q. Wei, and F. Gong, "Enhancing physical-layer security for IoT with nonorthogonal multiple access assisted semi-grant-free transmission," *IEEE Internet Things J.*, vol. 9, no. 24, pp. 24669–24681, Dec. 2022.
[47] M. V. Nguyen, D.-T. Do, F. Afghah, S. M. R. Islam, and A.-T. Le, "Exploiting secrecy performance of uplink NOMA in cellular networks," *IEEE Access*, vol. 9, pp. 95135–95154, 2021.
[48] J. Chen, L. Yang, and M.-S. Alouini, "Physical layer security for cooperative NOMA systems," *IEEE Trans. Veh. Technol.*, vol. 67, no. 5, pp. 4645–4649, May 2018.
[49] X. Li, M. Zhao, M. Zeng, S. Mumtaz, V. G. Menon, Z. Ding, and O. A. Dobre, "Hardware impaired ambient backscatter NOMA systems: Reliability and security," *IEEE Trans. Commun.*, vol. 69, no. 4, pp. 2723–2736, Apr. 2021.
[50] Q. Zhang, L. Zhang, Y.-C. Liang, and P.-Y. Kam, "Backscatter-NOMA: A symbiotic system of cellular and Internet-of-Things networks," *IEEE Access*, vol. 7, pp. 20000–20013, 2019.
[51] I. Csiszar and G. Tusnády, "Information geometry and alternating minimization procedures," in *Statistics and Decisions*, vol. 1, R. Dedewicz, Ed. Munich, Germany: Oldenbourg Verlag, 1984, pp. 205–237.
[52] X. Yue and Y. Liu, "Performance analysis of intelligent reflecting surface assisted NOMA networks," *IEEE Trans. Wireless Commun.*, vol. 21, no. 4, pp. 2623–2636, Apr. 2022.
[53] C. Huang, A. Zappone, G. C. Alexandropoulos, M. Debbah, and C. Yuen, "Reconfigurable intelligent surfaces for energy efficiency in wireless communication," *IEEE Trans. Wireless Commun.*, vol. 18, no. 8, pp. 4157–4170, Aug. 2019.
[54] L. N. Ribeiro, S. Schwarz, M. Rupp, and A. L. F. de Almeida, "Energy efficiency of mmWave massive MIMO precoding with low-resolution DACs," *IEEE J. Sel. Topics Signal Process.*, vol. 12, no. 2, pp. 298–312, May 2018.
[55] Y. Song, W. Yang, Z. Xiang, B. Wang, and Y. Cai, "Secure transmission in mmWave NOMA networks with cognitive power allocation," *IEEE Access*, vol. 7, pp. 76104–76119, 2019.
[56] I. S. Gradshteyn and I. M. Ryzhik, *Table of Integrals, Series, and Products*. New York, NY, USA: Academic, 2014.
[57] X. Wang, W. Chen, and Z. Cao, "A rateless coding based multi-relay cooperative transmission scheme for cognitive radio networks," in *Proc. IEEE Global Telecommun. Conf.*, Nov. 2009, pp. 1–6.
[58] X. Liu, "Average secrecy capacity of the Weibull fading channel," in *Proc. 13th IEEE Annu. Consum. Commun. Netw. Conf. (CCNC)*, Jan. 2016, pp. 841–844.

[59] T.-H. Vu, T.-V. Nguyen, and S. Kim, "Wireless powered cognitive NOMA-based IoT relay networks: Performance analysis and deep learning evaluation," *IEEE Internet Things J.*, vol. 9, no. 5, pp. 3913–3929, Mar. 2022.
[60] T.-V. Nguyen, T.-N. Tran, K. Shim, T. Huynh-The, and B. An, "A deep-neural-network-based relay selection scheme in wireless-powered cognitive IoT networks," *IEEE Internet Things J.*, vol. 8, no. 9, pp. 7423–7436, May 2021.
[61] T. N. Nguyen, B. V. Minh, D.-H. Tran, T.-L. Le, A.-T. Le, Q.-S. Nguyen, and B. M. Lee, "Security–reliability analysis of AF full-duplex relay networks using self-energy recycling and deep neural networks," *Sensors*, vol. 23, no. 17, p. 7618, Sep. 2023.
[62] T. N. Do, G. Kaddoum, T. L. Nguyen, D. B. da Costa, and Z. J. Haas, "Aerial reconfigurable intelligent surface-aided wireless communication systems," in *Proc. IEEE 32nd Annu. Int. Symp. Pers., Indoor Mobile Radio Commun. (PIMRC)*, Sep. 2021, pp. 525–530.
[63] X. Yue, Y. Liu, S. Kang, A. Nallanathan, and Z. Ding, "Exploiting full/half-duplex user relaying in NOMA systems," *IEEE Trans. Commun.*, vol. 66, no. 2, pp. 560–575, Feb. 2018.
[64] W. Zhao, G. Wang, S. Atapattu, T. A. Tsiftsis, and C. Tellambura, "Is backscatter link stronger than direct link in reconfigurable intelligent surface-assisted system?" *IEEE Commun. Lett.*, vol. 24, no. 6, pp. 1342–1346, Jun. 2020.
[65] K. Guo, R. Liu, X. Li, L. Yang, K. An, and Y. Huang, "Outage performance of RIS-assisted cognitive non-terrestrial network with NOMA," *IEEE Trans. Veh. Technol.*, vol. 73, no. 4, pp. 5953–5958, Apr. 2024.
[66] A.-T. Le, N. X. Ha, D.-T. Do, S. Yadav, and B. M. Lee, "Enabling NOMA in overlay spectrum sharing in hybrid satellite-terrestrial systems," *IEEE Access*, vol. 9, pp. 56616–56629, 2021.
[67] T. N. Nguyen, L.-T. Tu, P. Fazio, T. Van Chien, C. V. Le, H. T. T. Binh, and M. Voznak, "On the dilemma of reliability or security in unmanned aerial vehicle communications assisted by energy harvesting relaying," *IEEE J. Sel. Areas Commun.*, vol. 42, no. 1, pp. 52–67, Jan. 2024.
[68] G. C. Trichopoulos, P. Theofanopoulos, B. Kashyap, A. Shekhawat, A. Modi, T. Osman, S. Kumar, A. Sengar, A. Chang, and A. Alkhateeb, "Design and evaluation of reconfigurable intelligent surfaces in real-world environment," *IEEE Open J. Commun. Soc.*, vol. 3, pp. 462–474, 2022.
[69] M. H. Khoshafa, T. M. N. Ngatched, M. H. Ahmed, and A. R. Ndjiongue, "Active reconfigurable intelligent surfaces-aided wireless communication system," *IEEE Commun. Lett.*, vol. 25, no. 11, pp. 3699–3703, Nov. 2021.
[70] A. M. Mathai, R. K. Saxena, and H. J. Haubold, *The H-Function: Theory and Applications*. Berlin, Germany: Springer, 2009.

PHU TRAN TIN (Member, IEEE) was born in Khành Hòa, Vietnam, in 1979. He received the bachelor's and master's degrees from Ho Chi Minh City University of Science, in 2002 and 2008, respectively, and the Ph.D. degree from the Faculty of Electrical Engineering and Computer Science, VSB Technical University of Ostrava, Czech Republic, in 2019. He is currently a Lecturer with the Faculty of Information Technology, Ton Duc Thang University, Ho Chi Minh City, Vietnam. His major research interests include wireless communication in 6G, energy harvesting, performance of cognitive radio, physical layer security, and NOMA.

MINH-SANG VAN NGUYEN was born in Ben Tre, Vietnam. He is currently pursuing the master's degree in wireless communications. He worked with the Industrial University of Ho Chi Minh City, Vietnam. He has authored or co-authored over 22 technical papers published in peer-reviewed international journals (SCIE), three book chapter, and two conference papers. His research interests include electronic design, signal processing in wireless communications networks, non-orthogonal multiple access, reconfigurable intelligent surfaces, and physical layer security. He was a Reviewer of WCNC conferences, IEEE Access, *International Journal of Electronics*, *EURASIP Journal on Wireless Communications and Networking*, IEEE Transactions on Aerospace and Electronic Systems, IEEE Transactions on Consumer Electronics, and IEEE Transactions on Vehicular Technology.

TRAN TRUNG DUY (Member, IEEE) received the Ph.D. degree in electrical engineering from the University of Ulsan, South Korea, in 2013. In 2013, he joined the Posts and Telecommunications Institute of Technology, Ho Chi Minh City Campus (PTIT-HCM), as a Lecturer, where he has been an Associate Professor in wireless communications, since 2022. His major research interests include cooperative communications, cooperative multi-hop, cognitive radio, physical-layer security, energy harvesting, hardware impairments, and fountain codes.

BUI VU MINH was born in Dong Nai, Vietnam, in March 1991. He received the Graduate degree in electrical and electronic engineering from Nguyen Tat Thanh University, Ho Chi Minh City, Vietnam, in 2015, and the master's degree in electrical engineering from Ho Chi Minh City University of Technology and Education, Ho Chi Minh City, in 2019. In 2014, he joined the Faculty of Engineering and Technology, Nguyen Tat Thanh University, as a Laboratory Practice Management and then he became a Lecturer, in 2017. His major research interests include wireless networks, robot, artificial neural networks, and power electronics.

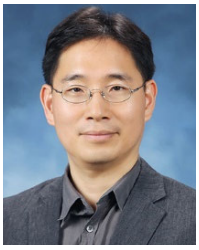

BYUNG-SEO KIM (Senior Member, IEEE) received the B.S. degree in electrical engineering from In-Ha University, South Korea, in 1998, and the M.S. and Ph.D. degrees in electrical and computer engineering from the University of Florida, in 2001 and 2004, respectively. His Ph.D. study was supervised by Dr. Yuguang Fang. Between 1997 and 1999, he was with Motorola Korea Ltd., South Korea, as a Computer Integrated Manufacturing Engineer in advanced technology research and development. From January 2005 to August 2007, he was with Motorola Inc., Schaumburg Illinois, as a Senior Software Engineer in networks and enterprises. His works have appeared in around 260 publications and 33 patents. His research interests include the design and development of efficient wireless/wired networks and distributed microservice computing. From 2012 to 2014, he was the Chairman of the Department of Software and Communications Engineering, Hongik University, South Korea, where he has been a Professor, since 2007. He is serving as an Associate Editor for IEEE Access, *Telecommunication Networks*, and *Journal of the Institute of Electronics and Information Engineers*. He also served as a Guest Editor of special issues for IEEE Internet of Things Journal (IEEE IoT), *International Journal of Distributed Sensor Networks*, IEEE Open Journal of the Communications Society (IEEE OJCS), IEEE Access, *Sensors*, *Applied Sciences*, and *Electronics*. He served as the general chair for international conferences.

LUBOS REJFEK was born in Chrudim, Czechoslovakia, in 1985. He received the Ph.D. degree from the Faculty of Electrical Engineering and Informatics, University of Pardubice, in 2017. He is currently a Lecturer with the Faculty of Electrical Engineering and Informatics and also employed with IAP CAS.